

Evidence for non-axisymmetry in M31 from wide-field kinematics of stars and gas ^{★,★★}

M. Opitsch^{1,2,3}, M.H. Fabricius^{1,2}, R.P. Saglia^{1,2}, R. Bender^{1,2}, M. Blaña¹, and O. Gerhard¹

¹ Max Planck Institute for Extraterrestrial Physics, Giessenbachstr., D-85748, Garching, Germany

² Universitäts-Sternwarte München, Scheinerstr. 1, D-81679, Munich, Germany

³ Excellence Cluster Universe, Boltzmannstr. 2, D-85748, Garching, Germany

Preprint online version: October 11, 2018

ABSTRACT

Aims. As the nearest large spiral galaxy, M31 provides a unique opportunity to learn about the structure and evolutionary history of this galaxy type in great detail. Among the many observing programs aimed at M31 are microlensing studies, which require good three-dimensional models of the stellar mass distribution. Possible non-axisymmetric structures like a bar need to be taken into account. Due to M31's high inclination, the bar is difficult to detect in photometry alone. Therefore, detailed kinematic measurements are needed to constrain the possible existence and position of a bar in M31.

Methods. We obtained ≈ 220 separate fields with the optical IFU spectrograph VIRUS-W, covering the whole bulge region of M31 and parts of the disk. We derive stellar line-of-sight velocity distributions from the stellar absorption lines, as well as velocity distributions and line fluxes of the emission lines H β , [OIII] and [NI]. Our data supersede any previous study in terms of spacial coverage and spectral resolution.

Results. We find several features that are indicative of a bar in the kinematics of the stars, we see intermediate plateaus in the velocity and the velocity dispersion, and correlation between the higher moment h_3 and the velocity. The gas kinematics is highly irregular, but is consistent with non-triaxial streaming motions caused by a bar. The morphology of the gas shows a spiral pattern, with seemingly lower inclination than the stellar disk. We also look at the ionization mechanisms of the gas, which happens mostly through shocks and not through starbursts.

Key words. galaxies: individual (Andromeda, M31, NGC224) – galaxies: Local Group – galaxies: bulges – galaxies: bar – galaxies: kinematics and dynamics – techniques: spectroscopic

1. Introduction

1.1. Recent surveys of M31

Because of its proximity, M31 is the best case after the Milky Way to learn about the detailed evolutionary history of a large spiral galaxy. Therefore, M31 has been studied by several major surveys in recent years, combining large-scale photometry with pointed spectroscopic observations. Two of these large programs are the Spectroscopic and Photometric Landscape of Andromeda's Stellar Halo survey (SPLASH) (Guhathakurta et al. 2005, 2006; Gilbert et al. 2006) and the Pan-Andromeda Archaeological Survey (PAndAS) (McConnachie et al. 2009). These surveys studied the stellar halo of M31 in great detail, to measure its global properties (Gilbert et al. 2012, 2014) and look at structures within the halo like the Giant Southern Stream (Gilbert et al. 2009). This provided information about the formation history of M31. One of the results of the PAndAS survey was that the dwarf galaxies around M31 all lie in a thin plane (Ibata et al. 2013), which poses problems for the current understanding of galaxy formation. The Panchromatic Hubble Andromeda Treasury (PHAT) program (Dalcanton et al. 2012)

looked at the disk of M31 and measured photometry for 117 million individual stars (Williams et al. 2014). The Herschel Exploitation of Local Galaxy Andromeda (HELGA) (Fritz et al. 2012) observed M31 in the far infrared and sub-millimeter wavelengths, measuring the distributions of dust (Smith et al. 2012) and molecular clouds (Kirk et al. 2015). Microlensing events and variable stars were monitored by the PAndromeda survey (Lee et al. 2012, 2014a,b).

All these surveys help to understand the structure, the accretion history and the history of star formation within M31.

M31 is classified as unbarred spiral SA(s)b by de Vaucouleurs et al. (1991), however, there has been evidence from photometry and kinematics that it is barred, see section 1.3. In this paper we present new spectroscopic observations of M31. The paper is focused on the description of the data and the hints for a bar that can be seen there. A discussion of other possible explanations, like a superposition of disks and rings, goes beyond the scope of this paper and will be presented in future papers based on the dataset described here.

1.2. Microlensing studies towards M31

The current Λ CDM paradigm (Planck Collaboration et al. 2016) has been very successful in explaining both the large scale structure of the universe and the observed properties of galaxies. One component of this model is the cold dark matter, which re-

* This paper includes data taken at The McDonald Observatory of The University of Texas at Austin.

** This research was supported by the DFG cluster of excellence 'Origin and Structure of the Universe'.

sides in halos around galaxies. The nature of this dark matter is not yet understood. The currently preferred candidates for dark matter are non-baryonic elementary particles, so-called WIMPs (Weakly Interacting Massive Particles), see e.g. Bertone (2010) and references therein. Baryonic candidates for dark matter are mostly ruled out, because the fraction of baryonic matter in the universe is only 15% of the total matter (Planck Collaboration et al. 2014). This baryonic dark matter fraction could be composed of large astrophysical objects, like brown dwarfs, Jupiter-sized planets or black holes, collectively known as Massive Astrophysical Compact Halo Objects (MACHOs) (Griest 1991). In order to place firm constraints on the existence of these massive objects, microlensing studies have been conducted. In such a microlensing event, a MACHO passes between a bright object and the earth, the light from the source objects is deflected by the gravity of the MACHO, which leads to a perceived increase in brightness of the source object. By observing such events, the number density of MACHOs can be determined (Paczynski 1986). The MACHO survey (Alcock et al. 1993) found that the contribution of MACHOs to the total halo mass of the Milky Way is 20% (Alcock et al. 2000), with an average MACHO mass of $\approx 0.4 M_{\odot}$. The EROS and EROS-2 projects (Aubourg et al. 1993; Afonso et al. 2003) measured a significantly lower fraction for the same masses, at less than 8% (Tisserand et al. 2007). The OGLE survey (Udalski et al. 1992) found a fraction that is comparable to the one measured by the EROS-survey (Wyrzykowski et al. 2011), less than 7% for MACHO masses lower than $1 M_{\odot}$. In addition to these results on the galactic halo, the galactic bulge microlensing surveys within OGLE-III (Wyrzykowski et al. 2015), MOA-II (Sumi et al. 2013) and EROS-2 (Hamadache et al. 2006) have become major tools for understanding the structure of the Milky Way, see e.g. Wegg et al. (2016) for a new analysis.

Several microlensing surveys have also been focused towards M31, like the Pan-STARRS 1 survey of Andromeda (PAndromeda) (Lee et al. 2012) and the Wendelstein Calar Alto Pixellensing Project (WeCAPP) (Lee et al. 2015). A total of 56 events have been detected in M31 (Lee et al. 2015). These events do not have to be caused by MACHOs, they can also happen due to lensing by other stars in M31, so-called self-lensing (Riffeser et al. 2006). To get an idea of the amount of events that are caused by self-lensing, a proper understanding of the three-dimensional distribution of the stars is needed. Models with different mass distributions of the galaxy result in widely varying predictions of the event rate of self-lensing and lensing through MACHOs. It is therefore important to model the stellar mass distribution in the galaxy as accurately as possible. Based on the data presented in this paper and numerical models from Blańa et al. (2017, hereafter B17) and Blańa et al. (in prep.), new predictions for microlensing events will be presented in a future paper (Riffeser in prep.).

1.3. The bar in M31

A large fraction of disk galaxies in the local universe is barred, ranging from about 50% in the optical (Barazza et al. 2008) to about 60% to 70% in the infrared (Eskridge et al. 2000; Menéndez-Delmestre et al. 2007). It is now thought that global instabilities in the disk lead to the quick formation of bars. In this process, the $m=2$ mode grows strongly by swing-amplification and forms a long-lasting bar non-linearly (Sellwood & Wilkinson 1993; Sellwood 2013). Over time, the inner part of the bar goes through a buckling phase, which is a short but violent vertical instability not long after bar for-

mation (Combes & Sanders 1981; Combes et al. 1990; Raha et al. 1991; Merritt & Sellwood 1994; Athanassoula & Misiriotis 2002; Debattista et al. 2005). The instability bends out of the plane of the disk, then settles back to the plane, redistributing energy to smaller spatial scales and to higher stellar velocity dispersion, thereby thickening the bar (Raha et al. 1991). The buckled part of the bar becomes a three-dimensional so-called boxy/peanut shaped (B/P) bulge, the part that has not buckled is referred to as the thin or flat bar. While this buckling phase is frequently seen in simulations, it has only recently been detected in observations by Erwin & Debattista (2016) for two local spiral galaxies.

While the Milky Way was originally thought of as unbarred, it is now widely accepted that it contains a bar. For a review, see Gerhard & Wegg (2015), and references therein. Recently, signs for a bar have also been detected in the innermost parts of the third large spiral galaxy in the Local Group, M33 (Hernández-López et al. 2009).

The question if M31 also contains a bar or not has not been settled, e.g. Widrow et al. (2003) refer to the bulge as “barlike”, while Kormendy et al. (2010) classify M31 as containing a classical bulge. If present, a bar is not easily detected in images of M31 because of its high inclination of 77° (Walterbos & Kennicutt 1987). This is too high to see a bar directly in the image, but too low to recognize its shape above and below the stellar disk, as is possible in an edge-on view (Athanassoula & Beaton 2006). Nevertheless, the boxy appearance of the isophotes in near-infrared images already is a hint at the existence of a bar (Beaton et al. 2007). However, boxy isophotes do not need to be caused by bars, there are numerous examples of early-type galaxies that are boxy without having a bar, see e.g. Kormendy et al. (2009).

It is possible to detect a bar in a galaxy with an inclination similar to the one of M31, Kuzio de Naray et al. (2009) investigated the galaxy NGC 2683 with a similar inclination to M31, by studying ionized gas velocities and the overall morphology. By combining the photometric and kinematic data, they found evidence for the presence of a bar in NGC 2683 and constrained its orientation and strength.

According to Stark & Binney (1994), there are three arguments for a triaxial structure in M31:

1. There is a twist in the inner isophotes in the bulge with respect to the outer disk, first seen by Lindblad (1956). He was subsequently the first one to claim that M31 has a bar. These twists cannot be reproduced by a rotationally symmetric distribution of stars (Stark 1977).
2. The velocities of the HI gas are not symmetric about the minor axis (Rubin & Ford 1971).
3. The ionized gas has the appearance of a spiral pattern, which is rounder than the appearance of the disk, as seen by Jacoby et al. (1985), Boulesteix et al. (1987) and Ciardullo et al. (1988).

Stark (1977) showed that the features measured by Lindblad (1956) can be explained by a family of triaxial bulge models. Stark & Binney (1994) narrowed down these models by simulating the velocities of the gas in this potential.

Berman (2001) and Berman & Loinard (2002) simulated the gas velocities in the triaxial bulge potential that was derived using the method of Stark (1977) and they are in agreement with the non-circular gas velocities in the inner disk. Their model has a fast pattern speed of $53.7 \text{ km s}^{-1} \text{ kpc}^{-1}$. Therefore, it would be more fitting to call their triaxial bulge a bar. In our understanding, a triaxial bulge would be a non-rotating structure. Most ob-

served bars have after the buckling phase a three-dimensional inner part of the bar, the B/P-bulge, and a flat outer part (see e.g. Athanassoula (2005) or Martinez-Valpuesta et al. (2006)). In this nomenclature, which we adopt throughout this paper, the “triaxial bulge” of the models by Berman (2001) and Berman & Loinard (2002) is a B/P-bulge. According to Gordon et al. (2006), the model by Berman (2001) explains the morphology of dust in M31, with spiral arms emerging from the bar. However, the fact that the two prominent dust rings do not share the same center, which also does not coincide with the optical center of M31, led Block et al. (2006) to propose a different scenario, where these rings were not created by a bar, but instead are shock waves due to the collision of the small companion galaxy M32 with M31.

Athanassoula & Beaton (2006) tested four different bar models and qualitatively compared the velocities to HI kinematics from Rubin & Ford (1970), Brinks & Shane (1984) and Brinks & Burton (1984), and the overall morphology to observations in the near infrared by Beaton et al. (2007). They found that in order to explain the boxy appearance of the isophotes in Beaton et al. (2007), a classical bulge needs to be present. The triaxial bulge seen by Lindblad (1956), Stark (1977) and Stark & Binney (1994), corresponds to the B/P bulge from Athanassoula & Beaton (2006). The fact that the boxy isophotes in Beaton et al. (2007) do not coincide with the disk argues for a misalignment of the bar and disk.

While the arguments for a bar in Athanassoula & Beaton (2006) are mostly qualitative, a more quantitative result was obtained by B17, who tested 84 different models and compared them to $3.6\mu\text{m}$ infrared photometry from Barmby et al. (2006), HI kinematics from Chemin et al. (2009) and Corbelli et al. (2010), as well as stellar kinematics from Saglia et al. (2010, hereafter S10) and data from the work presented in this paper. Again, they rule out solutions which do not contain a classical bulge component embedded within the B/P bulge, finding for the mass of the classical bulge $M_{\text{class}} = 1.0 - 1.4 \cdot 10^{10} M_{\odot}$ and for the half mass radius $r_{\text{class}} = 0.5 - 1.1$ kpc. In the preferred model in B17, the mass of the classical bulge component is $M_{\text{class,best}} = 1.1 \cdot 10^{10} M_{\odot}$ and the half-mass radius is $r_{\text{class,best}} = 0.53$ kpc, for the B/P component, the parameters are $M_{\text{B/P,best}} = 2.2 \cdot 10^{10} M_{\odot}$ and $r_{\text{B/P,best}} = 1.3$ kpc. The projected position angle of the bar is $PA_{\text{bar}} = 55.7^{\circ}$, which is 17.7° more than the disk position angle of $PA = 38^{\circ}$ (de Vaucouleurs 1958). The bar in the model by B17 started buckling about 2 Gyr after it formed, the buckling phase ended about 1 Gyr later. This happened at least 0.8 Gyr ago, but it could have happened earlier, because once the buckling phase is over, the galaxy evolves very slowly with time, so it can't be said when these events happened exactly. The intrinsic length of the bar is $1000''$, which projected onto the sky with M31's orientation and inclination becomes $600''$.

According to the models by Athanassoula & Beaton (2006) and B17, there are at least the following separate structural stellar components in M31, from the innermost to the outermost:

1. A classical spherical bulge in the center,
2. a B/P bulge, which is the inner thicker part of the bar,
3. a thin bar, this is the outer part of the bar,
4. a disk and
5. a halo.

This is the first paper in a series of papers about our observations of M31, this one covers the description of the data, the kinematics, and the gas fluxes, in an accompanying paper we will present results on the stellar populations. The data will also be made available online.

This paper is structured as follows: In section 2, our observations of M31 are described, before we present the methods used to fit the kinematics in section 3. Section 4 then presents the results for the stellar and gas kinematics, as well as the gas morphology. In section 5, we search for arguments for the bar in the data, before summarizing our findings in section 6.

We adopt a distance to M31 of 0.78 ± 0.04 Mpc (de Grijs & Bono 2014), an inclination of 77° (Walterbos & Kennicutt 1987) and a heliocentric velocity of -300 ± 4 km s^{-1} (de Vaucouleurs et al. 1991).

2. Observations

2.1. The IFU spectrograph VIRUS-W

The research of this project was carried out with the IFU spectrograph VIRUS-W (Fabricius et al. 2012a) mounted on the 2.7m telescope at the McDonald observatory. The integral-field unit consists of 267 fibers which are arranged in a rectangular hexagonal dense-pack scheme with a filling factor of 1/3. The field-of-view of the instrument is $105'' \times 55''$ at the 2.7m telescope, with the long edge of the fiberhead aligned along the east-west axis. Each fiber covers a circle with diameter $3.2''$ on sky. The actual spectrograph has two different resolution modes, each realized with a Volume Phase Holographic (VPH) grating. We use the high-resolution mode, where the grating has a line frequency of 3300 lines per millimeter and a resolution of $R \approx 9000$, which corresponds to an instrumental dispersion of $\sigma_{\text{inst}} = 15$ km s^{-1} . For a VPH a change of the grating angle results in an effective change of the blaze function, such that the throughput for a specific wavelength range is optimized. For our observations, we adjusted the grating angle to 353° after some testing to get moderately high throughput at the wavelength of $H\beta$ at 4861 \AA , with the maximum of the throughput being between 4900 \AA and 5100 \AA . The complete wavelength range is 4802 \AA to 5470 \AA . In this range, we see the emission lines $H\beta$ at 4861 \AA , the doublet of forbidden lines of doubly ionized oxygen [OIII] $\lambda\lambda 4959, 5007$ and the doublet of the forbidden nitrogen lines [NI] $\lambda\lambda 5198, 5200$.

2.2. Description of the observations

We observed 198 pointings in four separate observing runs, in October 2011, October 2012, February 2013 and August 2013. The positions of all observed pointings are shown in Fig. 1.

The observations consist of a completely covered area and six stripes extending further out. The angles of these stripes are 35° (approximately the disk major axis), 65° , 95° , 125° (approximately the disk minor axis), 155° and 185° . The completely covered region corresponds to the area where the bulge dominates the overall light (Kormendy & Bender 1999). Therefore, all pointings in the completely covered area will be called “bulge pointings” and the ones in the stripes “disk pointings”. Along the major axis, we reached approximately one disk scalelength of $r_d = 24' = 5.3$ kpc (Courteau et al.

² The image has been taken from http://archive.stsci.edu/cgi-bin/dss_form. The Digitized Sky Surveys were produced at the Space Telescope Science Institute under U.S. Government grant NAG W-2166. The images of these surveys are based on photographic data obtained using the Oschin Schmidt Telescope on Palomar Mountain and the UK Schmidt Telescope. The plates were processed into the present compressed digital form with the permission of these institutions. ©1995 by the Association of Universities for Research in Astronomy, Inc.

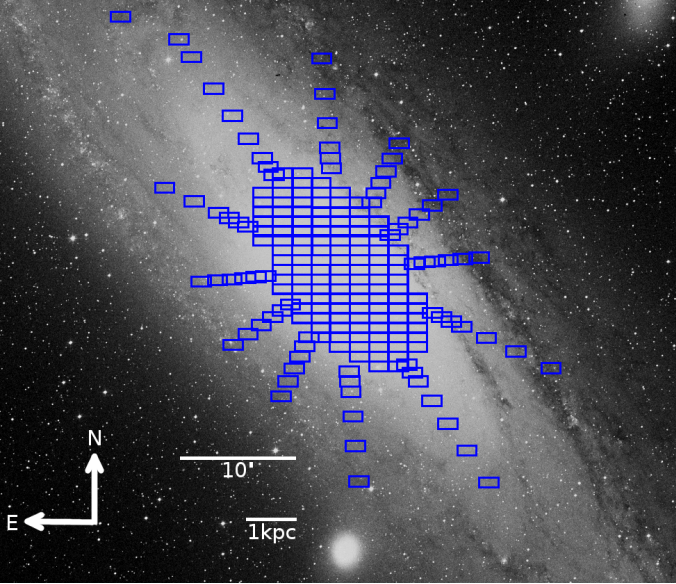


Fig. 1. Observed pointings of M31 overlaid on a Digitized Sky Survey² V-band image.

2011). We did not dither our observations, because we were primarily interested in covering a large area of M31 efficiently. We observed each galaxy pointing with an exposure time of 10 minutes, except for the central pointing, which was only observed for 5 minutes, because it covers the bright nucleus of M31, where sufficient signal-to-noise values were already reached with this shorter exposure time. Before and after each galaxy pointing, we nodded the telescope away from the galaxy to a sky position, which was exposed for 5 minutes. The seeing varied between 1.3'' and 3.0'' during the observations. At the beginning and at the end of each observation night, we took bias, flat and arc images.

2.3. Data reduction

The data reduction follows the standard procedure for VIRUS-W as described in Fabricius et al. (2014). It uses the `fitstools` package (Gössl & Riffeser 2002) and the `Cure` pipeline developed for HETDEX (Hill et al. 2004).

First, master biases, flats and arcs are created by taking the mean of the individual images for each morning and evening. The master bias frames are subtracted from all other frames.

`Cure` traces the fiber positions on the master flat frames and then extracts the positions of the spectral line peaks along these traces in the master arc frames. To model the distortion and the spectral dispersion, a two-dimensional seventh degree Chebyshev polynomial is used. The resulting model transforms between pixel positions on the detector and fiber-wavelength pairs and vice-versa.

Foreground stars, which appear as brightly illuminated fibers, are clipped using a κ - σ -clipping method.

For the wavelength calibration, 27 lines are used, they are listed in Table 1 in the Appendix.

Having traced the fiber positions and calibrated the wavelengths, the spectra are now extracted from the science frames by walking along the trace positions and averaging the values in a 7 pixel wide aperture. The extraction is performed in $\ln(\lambda)$ -space, the step width corresponds to 10 km s⁻¹.

The flatfield frames are extracted in the same way as the data frames.

The fiber to fiber throughput variation and the vignetting are corrected by dividing each observation by the corresponding flat-field observation. The flatfields are very stable over the course of one observing night, with the deviations being on the order of 0.03%. However, the resulting flat-fielded spectra still exhibit the rather strong variation of sensitivity as function of wavelength that is due to the strongly peaked diffraction efficiency of the VPH grating. This would complicate the later throughput calibration. Therefore, in the next step the spectra are divided at each wavelength by the mean value of the flat field spectrum at that wavelength, where the mean is taken across all fibers in the flatfield observation.

To take care of the sky, we pointed the telescope to a sky position before and after each galaxy pointing. The sky frames are fiber-extracted and flat-fielded in the same way as the galaxy observations. They are quite homogeneous after being flat-fielded, with a root-mean-square of the order of 1%. We average the two sky pointings observed before and after each galaxy pointing into one. The difference between the two sky pointings is very small, about 3%. We then subtract this flat-fielded sky image from the flat-fielded galaxy image.

Because the different observing runs took place in different months of the year, we also have to correct during the extraction for the relative motion of the earth around the sun. We use the web-tool by Edward Murphy³ based on an algorithm described in Meeks (1976) to calculate the relative velocity of the Earth towards M31 at the time of the observation. For each observing run, we use the value for the mean date of the run. We calculate the correction relative to the run in October 2011, because for that run, the correction is $c_{Oct11} = 0$ km s⁻¹. The correction for the run in October 2012 is $c_{Oct12} = -3.6$ km s⁻¹, for the run in February 2013 it is $c_{Feb13} = 19.1$ km s⁻¹ and for the run in August 2013 it is $c_{Aug13} = -28.1$ km s⁻¹.

The sky position for every fiber in each pointing of M31 is determined following Adams et al. (2011). The accuracy of this method was estimated by Adams et al. (2011) to be 0.21'', much less than the fiber diameter of VIRUS-W of 3.2''. The coordinates are converted to distance in arcseconds relative to RA=10:41:07.04 and DEC=41:16:09.41. This is the coordinate of the pointing covering the center of M31 in our observations.

In the central region, the signal-to-noise ratio (S/N) of each fiber spectrum lies well above 30. This remains true out to a radius of about 140'' along the major axis and 100'' along the minor axis. At larger radii fiber spectra are then spatially binned to reach a minimum S/N of 30 using the Voronoi-binning method by Cappellari & Copin (2003), resulting in a total of 7563 binned spectra.

3. Methods

3.1. Measuring the stellar kinematics with pPXF

The kinematics is measured using the routines pPXF (penalized PiXel Fitting) by Cappellari & Emsellem (2004) and GANDALF (Gas AND Absorption Line Fitting) by Sarzi et al. (2006). GANDALF uses pPXF as its first step. pPXF measures the stellar kinematics by broadening a weighted sum of template star spectra with a trial line-of-sight velocity distribution (LOSVD) and subsequently changing the parameters of the LOSVD un-

³ <https://www.astro.virginia.edu/~emm8x/utlils/vlsr.html>

til the residuals between the measured and the model spectrum are minimized. We use spectra from 41 kinematic standard stars obtained with VIRUS-W. They are listed in Table 2 in the Appendix. The information about the stars is taken from the ELODIE (Prugniel et al. 2007) and LICK (Worthey et al. 1994) catalogs. The coordinates come either from the ELODIE catalog or van Leeuwen (2007), using the SIMBAD interface (Wenger et al. 2000).

In PPXF, the LOSVD is expanded as a Gauss-Hermite series following van der Marel & Franx (1993) and Gerhard (1993):

$$\mathcal{L}(v) = \frac{\exp\left(-\frac{(v-\langle v \rangle)^2}{2\sigma^2}\right)}{\sigma\sqrt{2\pi}} \left[1 + \sum_{m=3}^M hm \cdot H_m\left(\frac{v-\langle v \rangle}{\sigma}\right) \right] \quad (1)$$

H_m are the Hermite polynomials and hm the Gauss-Hermite coefficients, the sum is broken off after M entries. We only look at the Gauss-Hermite moments $h3$ and $h4$.

3.2. Fitting the emission lines with GANDALF

The kinematics of the ionized emission lines are fitted with GANDALF (Sarzi et al. 2006). It fits the kinematics of the [OIII] λ 5007 line and ties the kinematics of the other emission lines to that line. In Fig. 2, a fit with GANDALF to a spectrum is plotted.

Close examination of the spectra shows that in many regions multiple gas components at different radial velocities exist. In order to properly treat these multiple peaks, we add another [OIII] component to be fitted with GANDALF. We also add a second $H\beta$ component and a second [NI] component. The initial guesses for the gas velocities have to be slightly different for the two components, otherwise GANDALF does not fit separate components. An example of a fit with two lines is shown in Fig. 3. Here, the two lines have almost the same amplitude and are clearly separated.

This is not always seen so clearly, there are also cases where one line is stronger than the other or where the two lines are almost blended together or where there is only one line clearly visible with a skewed line shape, that can, however, be described by the combination of two lines.

In Fig. 4, we show where we find one line and two lines. We see only one line in about 3000 bins, while we see two lines in about 3500.

In order to reliably fit the different components, we have to feed GANDALF information whether only one component is present or if it is really two. In order to get these initial guesses, we apply the following method: First, we cross-correlate a model spectrum only consisting of the [OIII] λ 5007 line with each spectrum. The program fits the resulting cross-correlation function with a set of Gaussians. These Gaussians all have the same dispersion of $\sigma = 20 \text{ km s}^{-1}$ and their peak velocities are 40 km s^{-1} apart. The program changes the amplitudes of the individual Gaussians to get the best approximation of the input cross correlated spectrum. We tell the program to only pick the Gaussian with the largest amplitude to have an estimate for the one-component fit and the one with the largest amplitude plus the one with the second largest amplitude for the two component estimate. If the amplitude of the second component is less than 0.25 times the amplitude of the first one, we decide to take the initial guess with only one component. We also discard unrealistically high velocity dispersions of $\sigma_{gas} > 100 \text{ km s}^{-1}$. We use the central velocities of the Gaussians as the initial guesses for GANDALF, letting it fit one line for the cases where we have found only one line and letting it fit two lines where we have found two

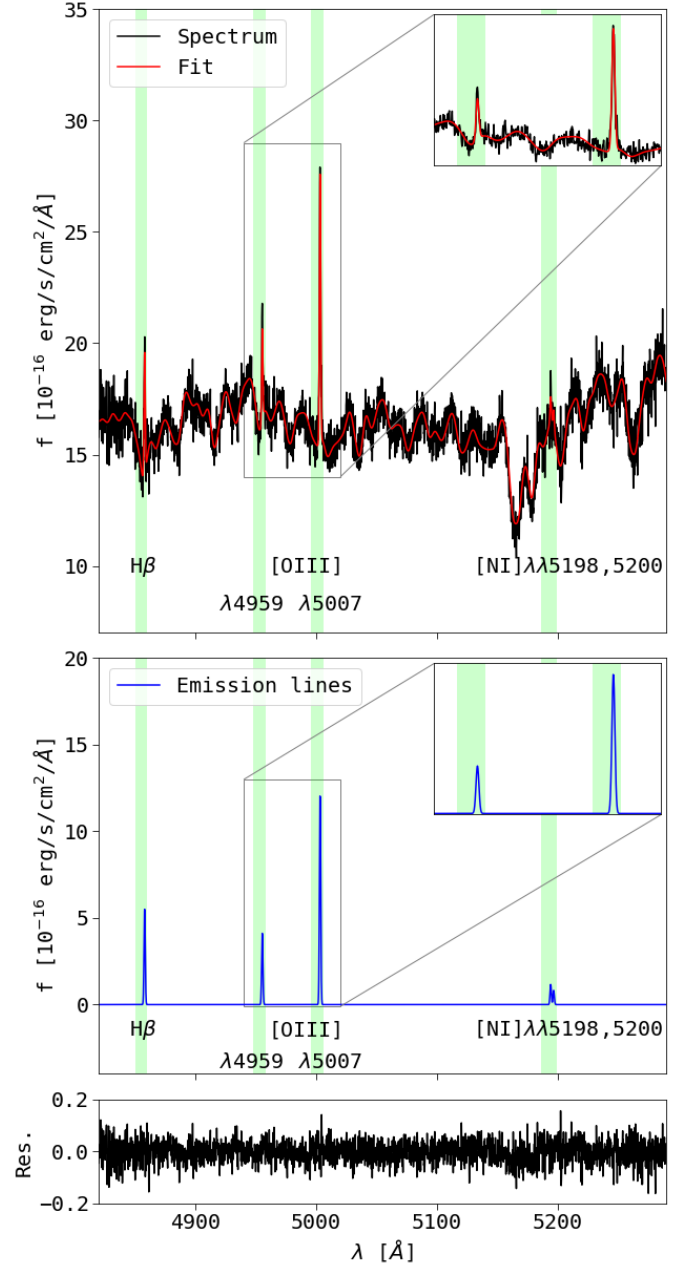


Fig. 2. A spectrum from the bulge region with the fit by GANDALF.

Top: Flux-corrected spectrum (black), best fit by GANDALF (red), which is the sum of the model stellar and the emission line spectra. The green shaded areas are the regions where the emission lines are expected. A zoom into the region of the [OIII] doublet is shown on the right.

Middle: The best fit emission lines with a zoom into the region of the [OIII] doublet.

Bottom: The residuals $(f_{measured} - f_{fitted})/f_{measured}$.

lines.

After a first iteration, we check all fits manually, update the initial guesses for the spectra where the fit failed and let GANDALF fit a second iteration. This second iteration results in 85 % of the spectra being fitted correctly, the rest is left out of the analysis.

In order to check if the spectra could be contaminated by a contribution of PNe, we looked at the catalogue of PNe positions

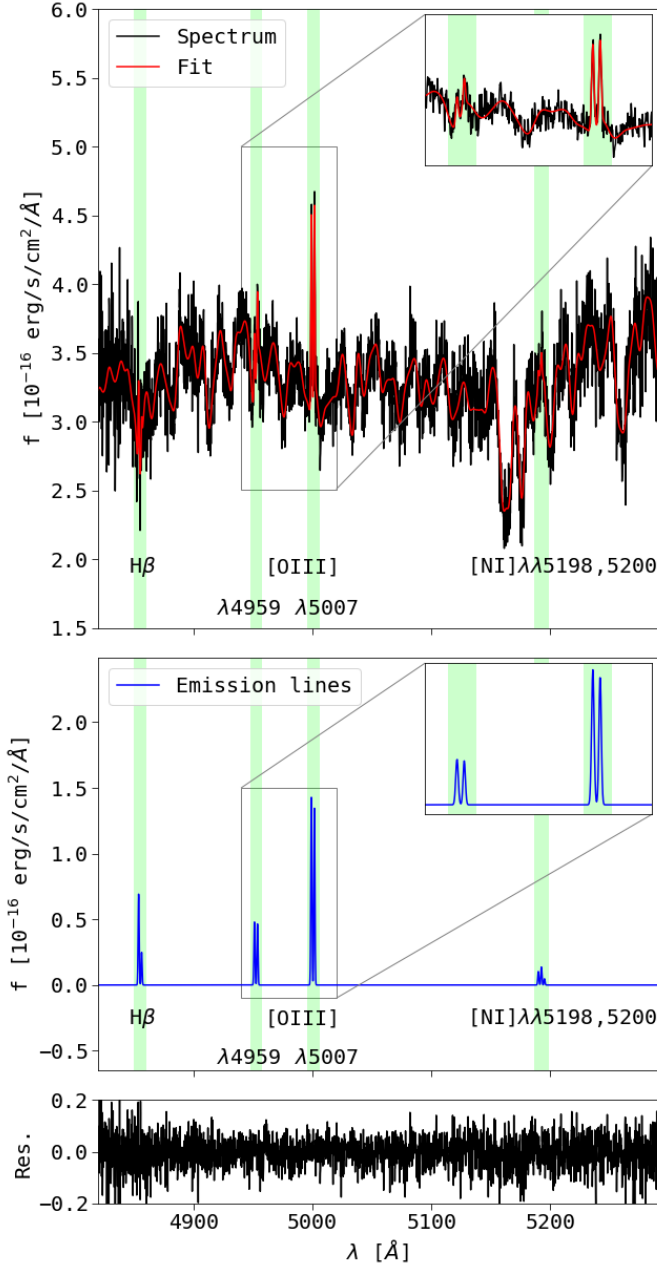


Fig. 3. A spectrum from the outer edges of the bulge region where the emission lines are split into two lines with almost equal amplitudes. The plot is analogous to Fig. 2.

from Merrett et al. (2006). If the position of a PNe is closer than $1.6''$ (the radius of a fiber), we see this bin as affected. Overall, 166 bins are affected, which is 2.5%. All of these spectra show [OIII] lines, about $2/3$ of them show two lines, while $1/3$ show only one line. The spectra do not look systematically different from the unaffected spectra, there is for example no exceptionally bright line in any of them. We therefore conclude that contamination by PNe is negligible.

3.3. Flux calibration

In each observation night, we observe photometric standard stars, they are listed in the appendix in Table 3. These spectra are compared to photometrically calibrated spectra from the litera-

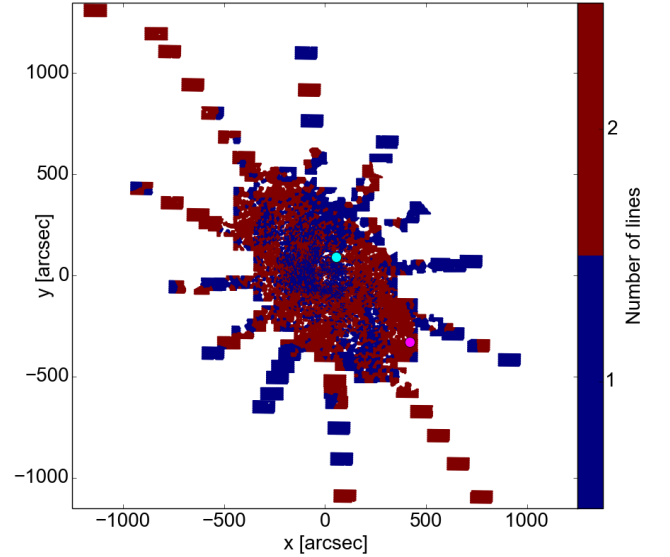


Fig. 4. Map of where the emission lines exhibit two peaks (red) and where they only have one (blue). The location of the spectrum with one peak from Fig. 2 is marked with the cyan dot, the location of the spectrum with two peaks from Fig. 3 is marked with the magenta dot.

ture (Oke 1990; Le Borgne et al. 2003) to get the throughput for the particular observation night as a function of wavelength. The throughput curves are calculated with a program from (Müller 2014), the error for the throughput curve is about 4%.

The atmospheric extinction is also corrected for each individual observation.

Differences in observing conditions between the individual pointings are taken into account by comparing the integrated flux f_{tot} in one spectrum to the flux f_V of a photometric model image. This image is constructed by combining the bulge-disk decomposition by Kormendy & Bender (1999) with an ellipse fit to a K-band image performed by S10. The model image is shown in Fig. 5.

GANDALF calculates $1-\sigma$ errors in the routine, which are consistent with what we obtain from Monte-Carlo simulations of fitting a noiseless spectrum with random added noise. These $1-\sigma$ errors are the ones tabulated in Table 6 in the appendix.

4. Results

4.1. Stellar Kinematics

In this section, the stellar kinematics measured with GANDALF is presented. The data will be made available online, an example table is given in Table 4 in the Appendix. We compare our data with the measurements by S10 in the appendix in section 7.1. In general, both datasets agree very well.

The stellar velocity map is plotted in Fig. 6, the heliocentric velocity of M31 ($v_{sys} = -300$ km/s; de Vaucouleurs et al. 1991) has been subtracted.

A schematic view of M31 based on Henderson (1979) is plotted in Fig. 7, with the naming of the receding and approaching sides of M31 taken from the stellar velocity map in Fig. 6. Overall, the stellar velocity field is regular, rotation is clearly visible. The velocities increase strongest along the disk major axis, with the highest velocity in the bulge region being $v_{bulge,max} = 136 \pm 4$ km s $^{-1}$ in the outermost bulge pointing in the receding

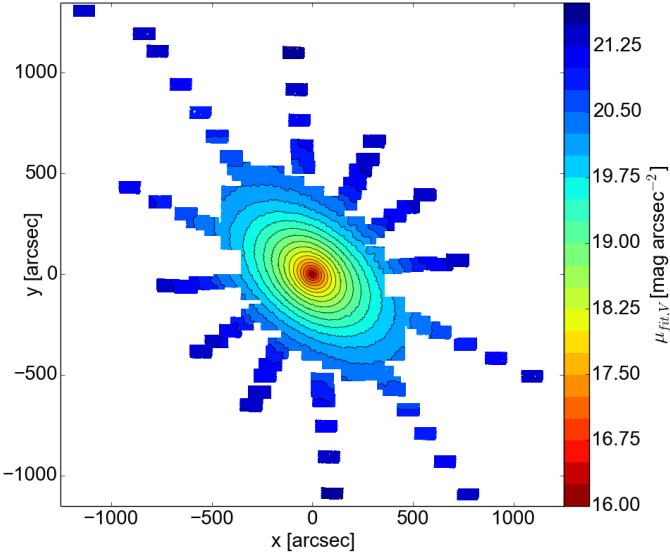


Fig. 5. Model image of M31, constructed by combining the V-band magnitude from the decomposition of (Kormendy & Bender 1999) with an ellipse fit to a K-band image by S10.

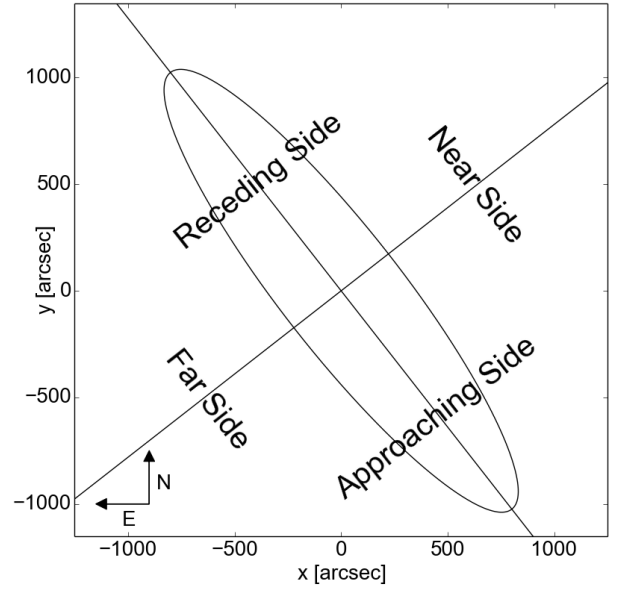


Fig. 7. Schematic view of M31. A generic ellipse with ellipticity $\epsilon = 0.78$ is plotted, this corresponds to an inclination angle of $i = 77^\circ$, the disk major axis has position angle $PA = 38^\circ$. The half of the galaxy to the north-west of the major axis is the near side (Henderson 1979).

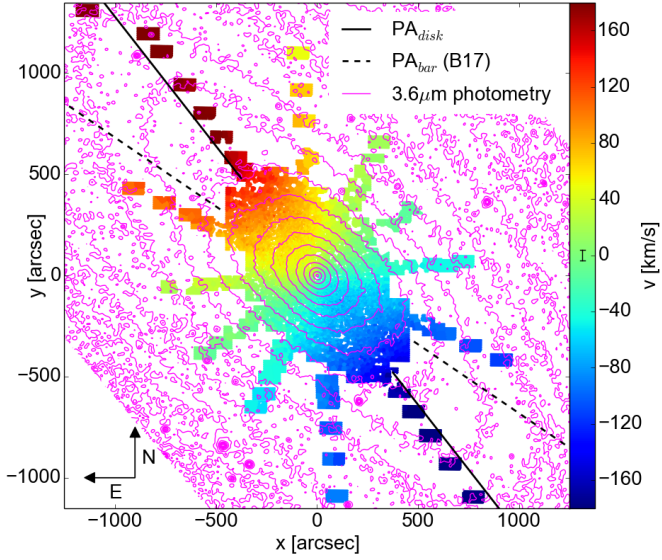


Fig. 6. Map of the stellar velocity corrected for the systemic velocity of M31. The solid straight line is the disk major axis at $PA_{disk} = 38^\circ$, the dashed straight line is the bar major axis at $PA_{bar} = 55.7^\circ$ from B17. The magenta contours are the surface brightness of the IRAC $3.6\mu\text{m}$ image by Barmby et al. (2006). The line in the colorbar is the median errorbar of the velocities.

side and the lowest being $v_{bulge,min} = -157 \pm 4 \text{ km s}^{-1}$ on the opposite side. The “bulge region” is the region of M31 where the bulge-to-total ratio of M31 is higher than 0.5, taken from a decomposition by Kormendy & Bender (1999). The absolute maximum of the velocities is reached with $v_{max} = 208 \pm 3 \text{ km s}^{-1}$ in the outermost disk major axis disk pointing in the receding side, and the lowest value of $v_{min} = -193 \pm 2 \text{ km s}^{-1}$ already reached in the disk pointing at a radius of $930''$ on the approaching side. On that side, the velocity roughly remains at that value to the outermost radii. The median velocity error is $dv = 3.8 \text{ km s}^{-1}$. When plotting the velocity map with contours, see Fig. 8,

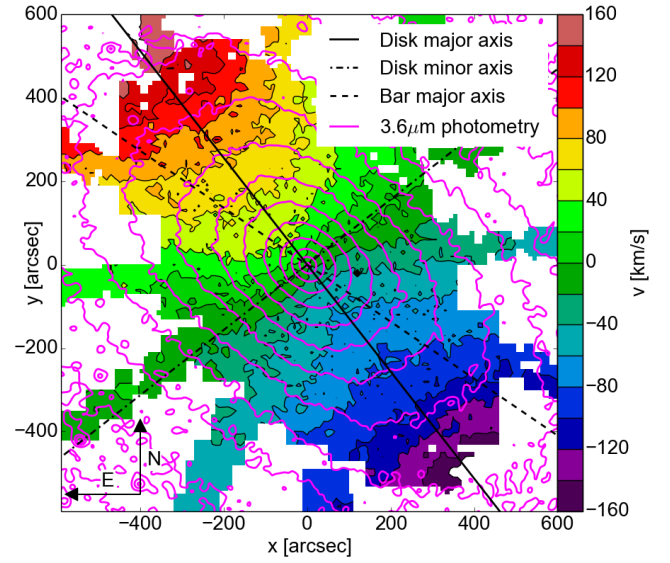


Fig. 8. The map of the stellar velocity from Fig. 6 plotted with contours. The solid line is the disk major axis (38°), the dash-dotted line the disk minor axis (128°) and the dashed line is the bar major axis (55.7°). The magenta contours are from the IRAC $3.6\mu\text{m}$ image. In this visualisation, the line of zero velocity shows a slight twist in the eastern half of the bulge.

a twist for the line of zero velocity becomes apparent, it is not aligned with the photometric minor axis.

The stellar velocity dispersion of M31 is plotted in Fig. 9. In the center, there are two lobes with high values of velocity dispersion of over 165 km s^{-1} (red regions in Fig. 9), which are separated by a line of lower velocity dispersion along the major axis of the bar. Around this we see a region with slightly lower values ($\approx 160 \text{ km s}^{-1}$) that has the shape of a small parallelogram

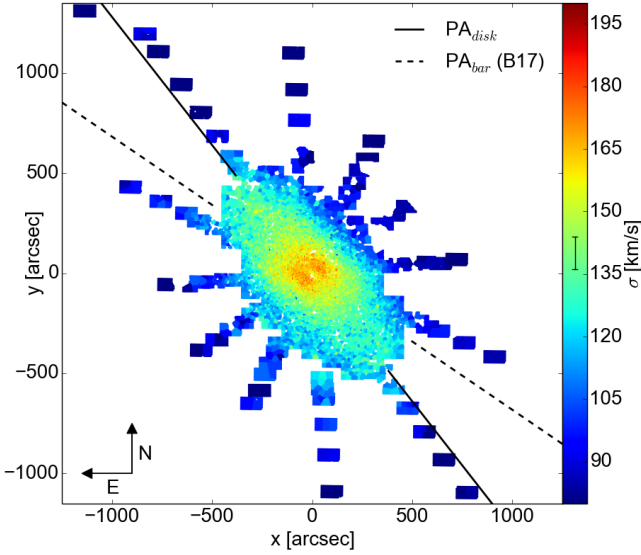


Fig. 9. Stellar velocity dispersion map with the disk major axis with $PA_{disk}=38^\circ$ (solid line) and the bar major axis with $PA_{bar}=55.7^\circ$ (dashed line) from the model by B17. The line in the colorbar is the median errorbar of the velocity dispersion.

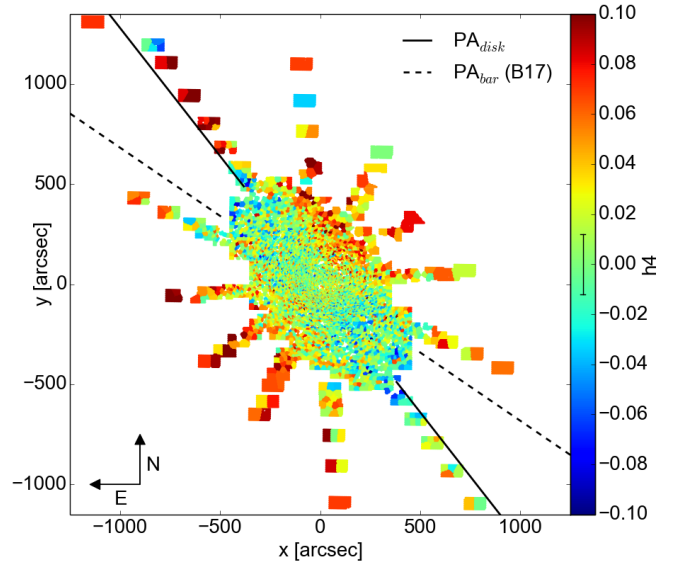


Fig. 11. Map of h_4 , the fourth moment in the Gauss-Hermite series. The lines are analogous to Fig. 9.

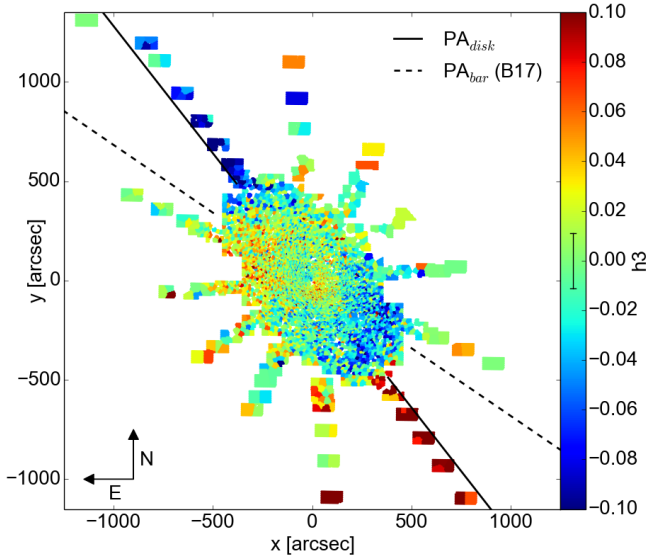


Fig. 10. Map of h_3 , the third moment of the Gauss-Hermite series. The lines are analogous to Fig. 9.

(yellow area in Fig. 9). Further out, we measure a region with even lower values of σ ($\approx 130 \text{ km s}^{-1}$), which is elongated along the disk major axis (light blue area in Fig. 9). σ drops faster along the disk minor axis than the major axis. The maximum value is $\sigma_{max} = 188 \pm 5 \text{ km s}^{-1}$, located at a distance of $46''$ from the center, the minimum value is $\sigma_{min} = 55 \pm 4 \text{ km s}^{-1}$, in the outermost northern disk pointing at $x=-100''$ and $y=1100''$. The mean velocity dispersion for the whole dataset is $\sigma_{mean} = 116 \pm 4 \text{ km s}^{-1}$, in the central $20''$ it is $\sigma_{central} = 160 \pm 5 \text{ km s}^{-1}$, considering only the bulge region it is $\sigma_{mean,bulge} = 137 \pm 4 \text{ km s}^{-1}$, in the disk it is considerably lower with $\sigma_{mean,disk} = 103 \pm 4 \text{ km s}^{-1}$. The disk velocity dispersion is still quite high, which is in agreement with what Fabricius et al. (2012b) have found for other disk galaxies.

In Fig. 10, we plot the Gauss-Hermite moment h_3 . In the very central $100''$, h_3 has high positive and negative values, while further out, the absolute values become lower. Further out in the bulge, the absolute values become higher again. In the disk along the major axis, the signs of h_3 flip and even higher absolute values are reached. Corresponding regions of high and low values are relatively symmetric with respect to the center. In the central $50''$, h_3 has values of about ± 0.05 . Further out, the values drop to about ± 0.02 , before rising at the edges of the bulge region to ± 0.08 . In the bulge, the mean absolute value is $|\overline{h_{3,bulge}}| = 0.03 \pm 0.02$. In the disk, the values are higher, the mean absolute disk value is $|\overline{h_{3,disk}}| = 0.04 \pm 0.03$. Along the disk major axis, the values are highest, here, the mean absolute value is $|\overline{h_{3,major}}| = 0.07 \pm 0.02$. The maximum and minimum values of the whole map are also found along the disk major axis, being $h_{3,max} = 0.14 \pm 0.02$ and $h_{3,min} = -0.16 \pm 0.02$. Over most of the bulge region, we see a correlation between h_3 and v , this will be discussed in section 5.

In Fig. 11, the Gauss-Hermite moment h_4 is presented. This map shows that along the disk major axis, the absolute values of h_4 are very low. At the ends of the bulge region, the values of h_4 become negative. Perpendicular to the disk major axis, the values of h_4 become positive. The mean value over the whole dataset is $\overline{h_4} = 0.02 \pm 0.02$. In a $240''$ wide and $350''$ long strip along the disk major axis, the mean value is lower, at $\overline{h_{4,outer\ bulge}} = 0.002$. Along the disk minor axis, the values of h_4 are generally higher, in regions that have a distance to the disk major axis of more than $120''$, the mean value is $\overline{h_{4,minor}} = 0.03$. In the disk pointings along the disk major axis, h_4 is higher in the northern half of the galaxy, having a mean value of $\overline{h_{4,major,north}} = 0.04$, while in the southern half, it is $\overline{h_{4,major,south}} = -0.01$.

4.2. Gas kinematics

In this section, the kinematics of the ionized gas is presented. These data will be made available online, an example table is given in table 5 in the Appendix. The motions of the gas are more complicated than the ones of the stars from section 4. More

complicated gas kinematics are often observed in disk galaxies (e.g. Falc3n-Barroso et al. (2006); Ganda et al. (2006)), because contrary to the dissipationless stars, the gas can also lose energy through radiation. The dense gas traced by ground-state CO and HI transitions is most likely to have settled onto closed orbits via hydrodynamic interactions. Associated with this dense gas are regions of ionized gas (Stark & Binney 1994), which is then seen in the optical emission lines. As mentioned in section 2, we see in about half of the investigated binned spectra two gas components separated in velocity. We tried several ways to sort the two components, e.g. sorting the components by flux or proximity in position space. In the end, we settled on sorting by velocity, because it produced the smoothest maps. The velocity map of the first component, which is the faster one of the two, is plotted in Fig. 12, the one of the second component in Fig. 13. The first gas component has a median absolute value of $|v_{[OIII,1]}|=162 \pm 5 \text{ km s}^{-1}$. The maximum value is $v_{[OIII,1],max} = 294.7 \pm 4.5 \text{ km s}^{-1}$ at the coordinates $(-220'', 281'')$, at $360''$ from the center along the disk major axis in the receding side. The minimum value is $v_{[OIII,1],min} = -340 \pm 3.0 \text{ km s}^{-1}$ at the coordinates $(25'', -100'')$, which is at about $100''$ south of the center in the approaching side, is closer to the center than the maximum on the other side, leading to an asymmetric appearance with respect to the center. Apart from that, there is a ‘‘spiral-like signature’’ in the inner-most $100'' \times 100''$ and a large ‘‘S-shape’’ between the approaching and receding gas velocities. These structures are marked in the zoomed-in inset of figure 12.

For the second component, the median absolute value is significantly lower than for the first component, with $|v_{[OIII,2]}|=73.2 \pm 5.5 \text{ km s}^{-1}$. The maximum value is $v_{[OIII,2],max} = 183.8 \pm 5.2 \text{ km s}^{-1}$ at the coordinates $(-190'', 280'')$, which is in the same region as the maximum for the first component. The minimum value is $v_{[OIII,2],min} = -240.2 \pm 3.8 \text{ km s}^{-1}$, at the coordinates $(65'', -170'')$, at $182''$ from the center along the disk major axis in the receding side. This again corresponds to a region of low velocities in the first component. The overall shape of the velocity field for the second component is similar to the first, also with an ‘‘S-shape’’ along the line of zero velocity. This structure has a slightly different shape than the one for the first component, an arm of approaching velocities is extending further into the region of receding velocities. Additionally, on the western side of the bulge, at about $500''$ along the disk major axis from the center, there is an arm of velocities of about zero. This arm seems to be unconnected to the kinematics of the rest of this component. These structures are marked in the zoomed-in inset of Fig. 13

The velocity dispersion of the first component is plotted in Fig. 14. The general appearance is noisy, overall, the mean value is $\overline{\sigma_{[OIII,1]}} = 35 \pm 5 \text{ km s}^{-1}$. The velocity dispersion is low near the northern end of the bulge along the major axis, where the velocities are high ($\sigma \approx 50 - 60 \text{ km s}^{-1}$).

In the velocity dispersion values of the second component, a ring-like structure of high values is visible, which increases the mean value of the velocity dispersion to $\overline{\sigma_{[OIII,2]}} = 37 \pm 6 \text{ km s}^{-1}$. The values in the ring are $\overline{\sigma_{[OIII,2]}} = 57 \pm 10 \text{ km s}^{-1}$. This ring of high velocity dispersions corresponds to a similar ring in Fig. 4, which is where two peaks are measured. In this ring, a second peak with a lower amplitude than the first peak is present. However, this second peak is broader, therefore the velocity dispersion is larger.

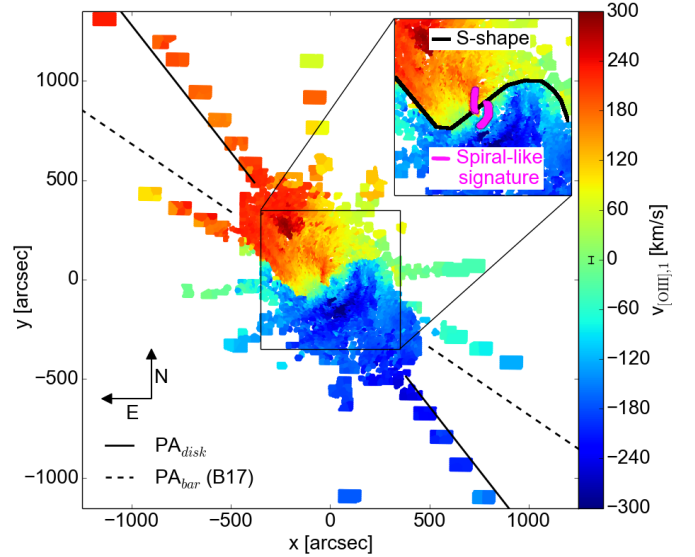


Fig. 12. Velocity map of the more rapidly rotating gas component 1. The lines are analogous to Fig. 9. The inset shows a zoom into the inner regions, with the ‘‘S-shape’’ highlighted along the line with systemic velocity. The ‘‘spiral-like signature’’ is highlighted with the magenta line, which encompasses both arms of the spiral. Both these structures are mentioned in the text.

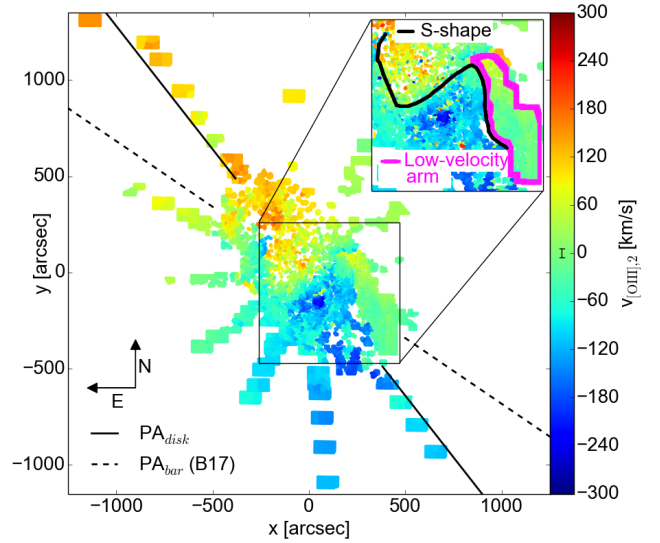


Fig. 13. Velocity map of the more slowly rotating gas component 2. The lines are analogous to Fig. 9. The inset shows a zoom into the inner regions, with the ‘‘S-shape’’ and the ‘‘low-velocity arm’’ highlighted, which are mentioned in the text.

4.3. Gas fluxes

The fluxes of $H\beta$, $[OIII]\lambda 5007$ and $[NI]\lambda 5198$ are plotted in Figs. 16 to 24. The values will be made available online, an example table is given in Table 6 in the Appendix. In Fig. 16 and Fig. 17, we show the line flux of the first and second $H\beta$ line, while in Fig. 18, we show the sum of the two components. The corresponding fluxes for $[OIII]\lambda 5007$ are shown in Fig. 19, Fig. 20, and Fig. 21. The plots for $[NI]\lambda 5198$ are plotted in Fig. 22, Fig. 23 and Fig. 24.

There are regions where the first component has higher flux than

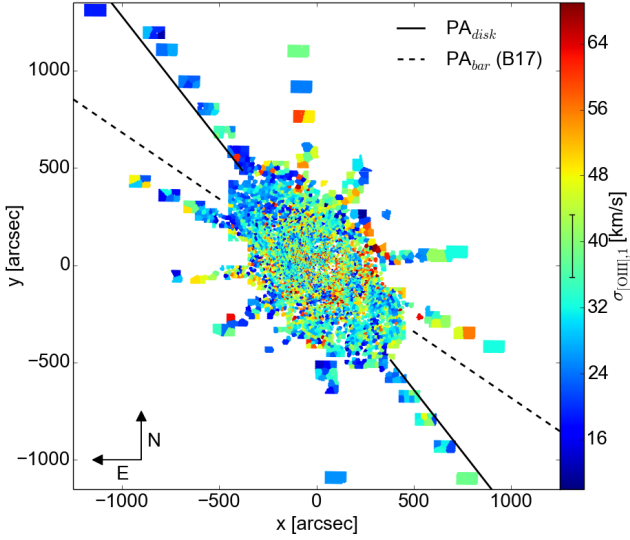


Fig. 14. Velocity dispersion of the first gas component. The lines are analogous to Fig. 9.

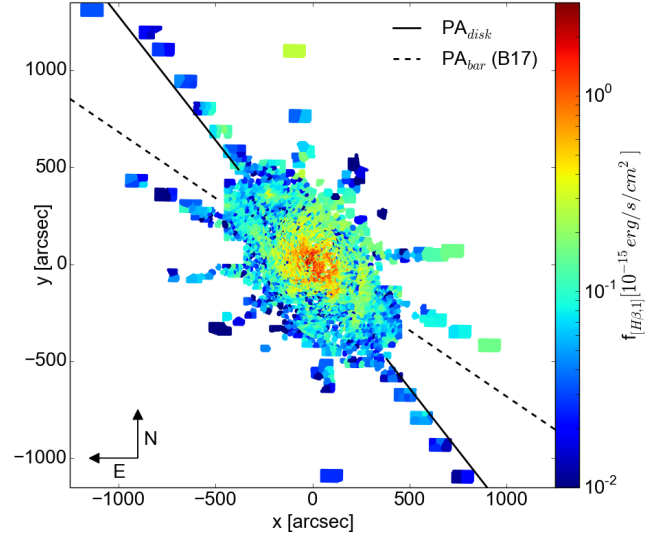


Fig. 16. Flux of first $H\beta$ component. The median error is $0.01 \cdot 10^{-15}$ [erg/s/cm²]. The lines are analogous to Fig. 9.

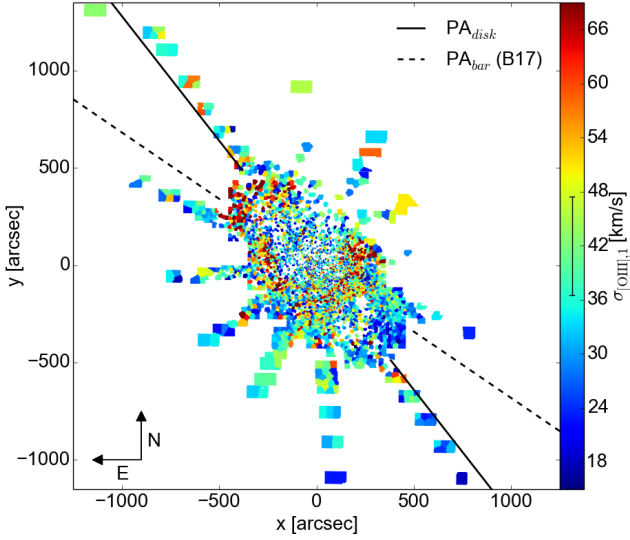


Fig. 15. Velocity dispersion of the second gas component. The lines are analogous to Fig. 9.

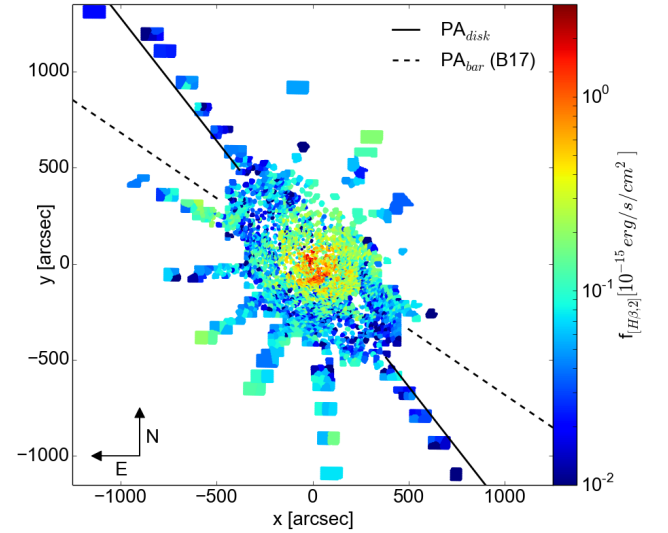


Fig. 17. Flux of second $H\beta$ component. The median error is $0.01 \cdot 10^{-15}$ [erg/s/cm²]. The lines are analogous to Fig. 9.

the second one, as well as regions where the opposite is true. When averaging the fluxes along ellipses, however, it becomes apparent that the first component is stronger than the second one. This is true for all different lines. In the $H\beta$ and [OIII] maps, a spiral structure is visible over most of the bulge region, with an incomplete elliptical ring inside, which is oriented roughly along the minor axis, with a “spoke” along the ring’s short axis. The ring and spoke are highlighted in the zoomed-in inset of Fig. 18. This ring is at a smaller radius than the one mentioned above in the velocity dispersion of the second gas component. In the southwest, one of the arms of the spiral pattern is prominent in the $H\beta$ and the [OIII]. The fluxes of $H\beta$ are lower than the ones of [OIII]. The [NI] is much fainter than either the $H\beta$ or the [OIII], no clear pattern can be seen there apart from the fact that it becomes brighter in the center. The overall filamentary appearance of the gas morphology could be either due to heating by shocks or supernovae of type Ia (Jacoby et al. 1985).

We did ellipse fits to the maps of the [OIII] gas and compared it to the stellar surface brightness. The comparison is shown in Fig. 25. From about $30''$ to about $200''$, the decline of the [OIII] is similar to the one of the stars, while further out, it drops significantly compared to the light of the stars. This corresponds to the edge of the spiral structure visible in the maps. The second [OIII] component has lower flux values, its profile is more irregular, but it also declines fast from $200''$ outwards.

5. Bar signatures in kinematics and morphology

5.1. Bar signatures in the stellar kinematics

A bar leaves certain signatures in the kinematics of the stars. Bureau & Athanassoula (2005) modeled several bars, with different strengths and viewing angles. Stark & Binney (1994), Athanassoula & Beaton (2006) and B17 all find that the bar in M31 is neither viewed end-on nor side-on, but instead at an in-

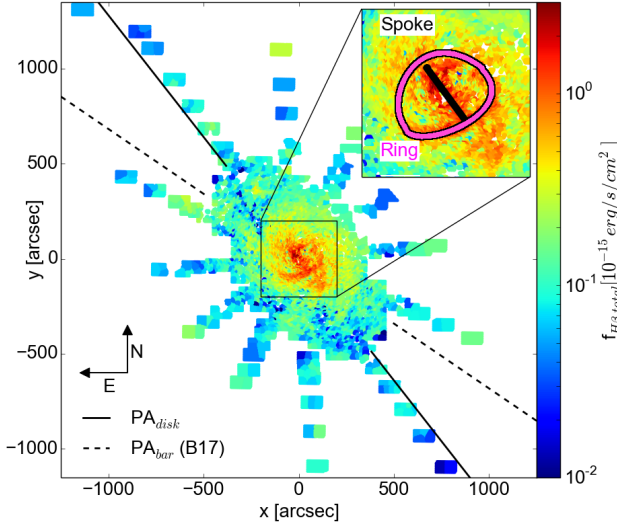


Fig. 18. Flux of both $H\beta$ components combined. The median error is $0.02 \cdot 10^{-15}$ [erg/s/cm²]. The lines are analogous to Fig. 9. The inset shows a zoom into the inner $200'' \times 200''$, with the structures “ring” and “spoke” highlighted, which are mentioned in the text.

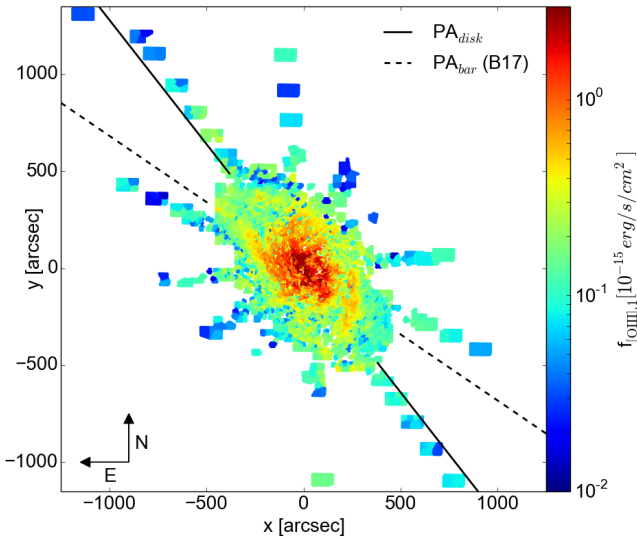


Fig. 19. Flux of first [OIII] component. The median error is $0.01 \cdot 10^{-15}$ [erg/s/cm²]. The lines are analogous to Fig. 9.

intermediate angle. The special signatures of a bar are plateaus in the velocity and the velocity dispersion, and minima in the higher moments h_3 and h_4 . These were theoretically predicted by Bureau & Athanassoula (2005) and measured on several barred galaxies by Chung & Bureau (2004). We adopt the model of B17 as the one against which we compare our results. In their model, the bar has a position angle of $PA_{bar}=55.7^\circ$, extending out to $600''$ in projection. However, in the direction of the bar, our coverage only extends to $500''$, we are therefore missing the crucial regions of the end of the bar. Pointings covering these regions are being observed and the results will be presented in a future paper. The co-rotation radius of B17 and the outer Lindblad resonance are also outside our observed regions.

In Fig. 26, cuts through the kinematic fields along the disk major axis are plotted. Left corresponds to the north-eastern re-

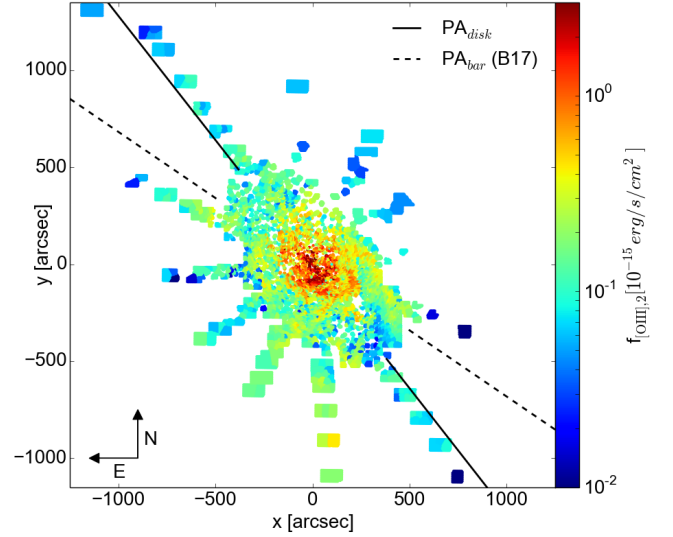


Fig. 20. Flux of the second [OIII] component. The median error is $0.01 \cdot 10^{-15}$ [erg/s/cm²]. The lines are analogous to Fig. 9.

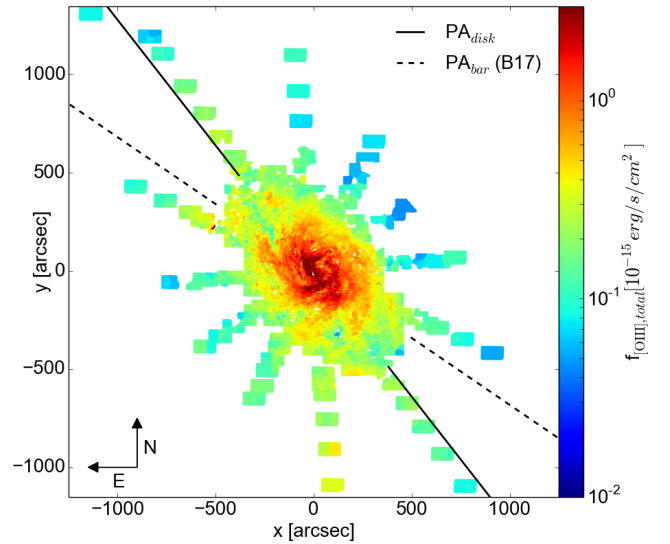


Fig. 21. Sum of the flux of the two [OIII] components. The median error is $0.02 \cdot 10^{-15}$ [erg/s/cm²]. The lines are analogous to Fig. 9.

ceding side, right to the south-western approaching side. The velocity rises to 70 km s^{-1} at $35''$, before remaining relatively constant until $350''$ on the left and $460''$ on the right, before reaching 160 km s^{-1} at $-750''$ on the left and at $660''$ on the right. An axisymmetric stellar disk rises rapidly, but smoothly and remains flat at large radii. Bureau & Athanassoula (2005) found that a bar seen end-on produces a “double-hump” profile, where the velocity rises rapidly to a local maximum, then drops slightly to create a local minimum and then rises again slowly to the flat section at the end. When the bar is not seen end-on, but at an intermediate angle, this behavior is weakened and the local maximum and minimum disappear and form a single plateau at moderate radii, which is what we see in the profiles of M31. This is expected from the models by B17, where the bar is seen at an intermediate angle. The rising part of the velocity curve comes from the orbits of the stars that are parallel to the bar, while the slower growth afterwards, or the local minimum in the case of

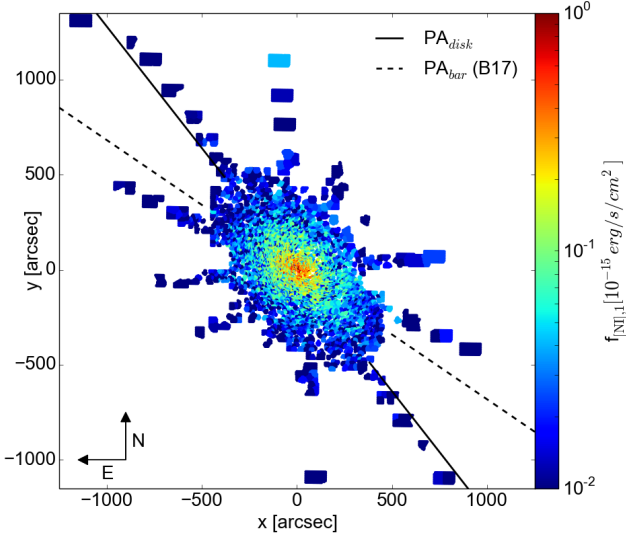


Fig. 22. Flux of the first [NI] component. The median error is $0.01 \cdot 10^{-15}$ [erg/s/cm²]. The lines are analogous to Fig. 9.

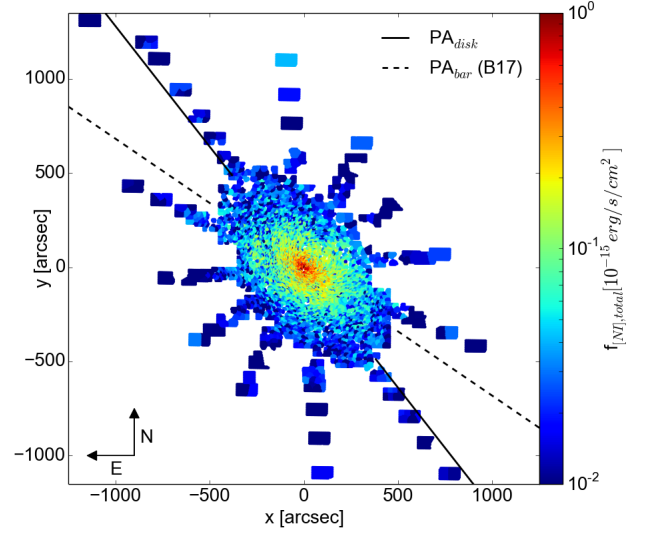


Fig. 24. Total flux of the two [NI] components. The median errorbar is $0.01 \cdot 10^{-15}$ [erg/s/cm²]. The lines are analogous to Fig. 9.

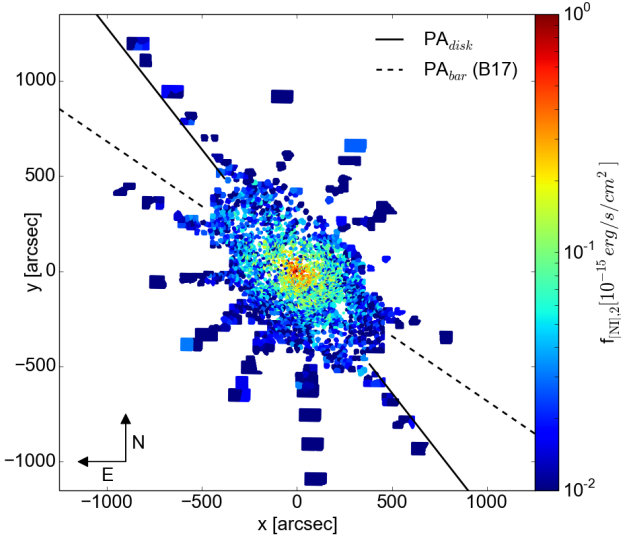


Fig. 23. Flux of the second [NI] component. The median error is $0.01 \cdot 10^{-15}$ [erg/s/cm²]. The lines are analogous to Fig. 9.

an end-on bar, is caused by an inner ring structure caused by the bar (Bureau & Athanassoula 2005).

The velocity dispersion profile in Fig. 26 shows that σ has two off-centered maxima, with a slight drop of about 8 km s^{-1} in between. This drop was first observed by Kormendy (1988), who saw them as evidence for a central disk and subsequently the supermassive black hole. Bureau & Athanassoula (2005) find that such minima can also be caused by the bar, because the orbits parallel to the bar become more circular and thus lower the dispersion, however, the minimum in models by Bureau & Athanassoula (2005) is usually much stronger than what we measure here. One should keep in mind that such minima are not uniquely related to bars. Comerón et al. (2008) suggested that cold gas is accreted to the center and a subsequent starburst creates then stars with low velocity dispersion. They claim that the gas is most probably driven into the center by spiral arms, but also, albeit less probable, bars.

An inner disk can also lead to this minimum, such a structure has

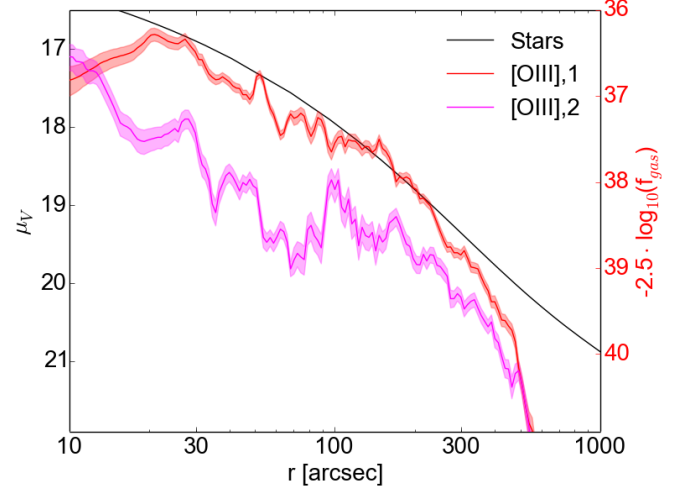


Fig. 25. Comparison of the surface brightness of the stars (black) taken from Kormendy & Bender (1999) with ellipse fits to the fluxes of the first [OIII] component (red) and the second [OIII] component (magenta). The left y-axis is valid for the stellar surface brightness, the one on the right for the fluxes of the two gas components. The scales have been adjusted so that the profiles for the stars and the first [OIII] component can be compared easily.

been found in the very center of M31 (Tremaine 1995; Peiris & Tremaine 2003), however, with a scalelength of only about $1''$, this structure is not resolved by our observations. The drop could also be caused by the classical bulge (B17). σ drops to 140 km s^{-1} at $400''$, before staying roughly constant out to $600''$ and then reaching 80 km s^{-1} at $950''$. These plateaus, which are not completely flat, but only less inclined than the rest of the profile, are also frequently seen in barred galaxies (Bureau & Athanassoula 2005).

The $h3$ profile in Fig. 26 shows that the slope of $h3$ changes sign several times. The maxima and minima in the $h3$ correspond to the points where the slope of the velocity profile changes, this is similar to the behavior of the simulations by Bureau

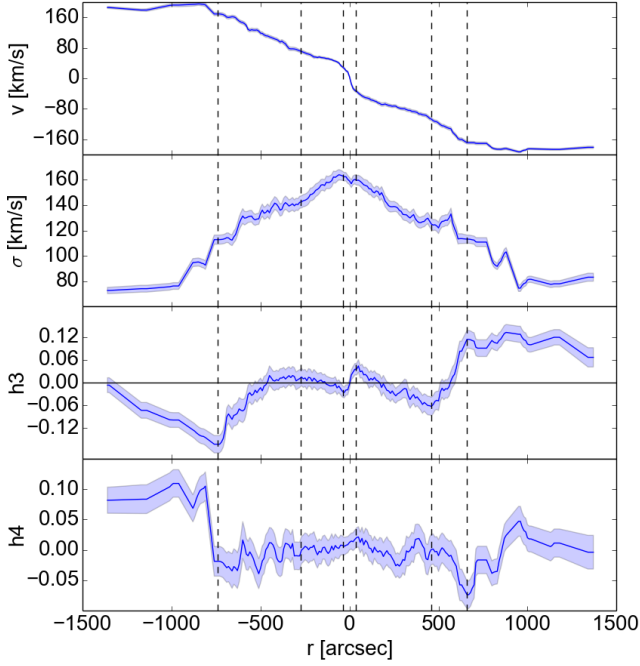


Fig. 26. Cuts through the stellar kinematic maps from VIRUS-W along the disk major axis ($PA=38^\circ$). In the third panel, the horizontal line is $h3=0$. The vertical dashed lines highlight the position where $h3$ has a local maximum or minimum.

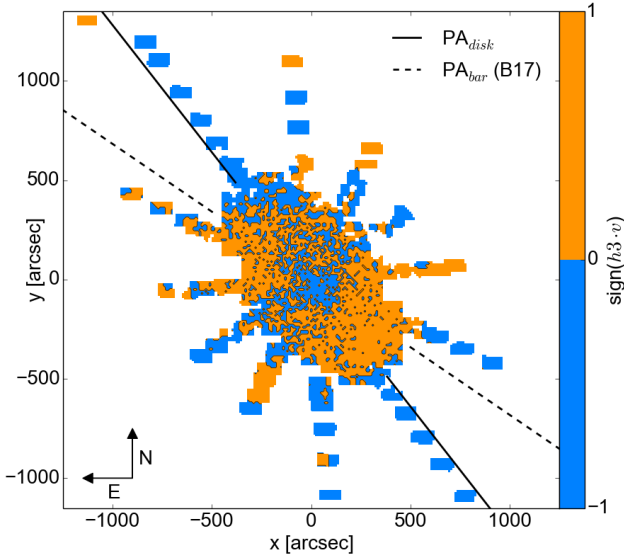


Fig. 27. Correlation between the stellar velocity and $h3$. Plotted is $\text{sign}(h3 \cdot v)$, with the disk and bar major axis from Fig. 9.

& Athanassoula (2005) and has also been observed in barred galaxies (Fisher 1997; Chung & Bureau 2004; Falc3n-Barroso et al. 2006; Ganda et al. 2006). In Fig. 27, we show the correlation between $h3$ and v . The color blue represents where the two quantities are anti-correlated, while in orange areas, they are correlated. In the outer regions, $h3$ is anti-correlated to v , which is the expected behavior for disky structures in a galaxy (Binney & Tremaine 1987; Bender et al. 1994; Fisher 1997; Binney & Tremaine 2008). In the central $30''$, $h3$ is again anti-

correlated to the velocity. This could mean that a disky structure is also present at the center, potentially explaining the slight drop in velocity dispersion. The radial extent of this central anti-correlation corresponds roughly to the rapidly rising part of the rotation curve, a behavior that is also seen in other disk galaxies (Chung & Bureau 2004) and interpreted as a decoupled inner disk. In between the two anti-correlated regions, $h3$ becomes correlated with the velocity, which is taken by Bureau & Athanassoula (2005) to be a sign for a bar. The correlated region is oriented more along the bar major axis than the disk major axis. It is more prominent in the south-west than in the north, because the northern edge of the bulge is more affected by dust (Draine et al. 2014). The correlation means that there are more stars rotating faster than the circular velocity in projection, which may be a consequence of elongated motions. However, the correlation does not necessarily have to be caused by a bar, it can also be caused by the superposition of an axisymmetric bulge component embedded in a rotating disk, depending on the bulge-to-disk ratio. If the bulge is brighter than the disk, the main velocity that is seen is mainly the bulge, with the disk creating a tail of high-velocity material (van der Marel & Franx 1993; Bureau & Athanassoula 2005).

The $h4$ profile in Fig. 26 is relatively constant, with the exception of a minimum at $670''$, where $h4$ drops from 0 to -0.07 . This minimum corresponds to the radius where $h3$ reaches its maximum. On the opposite side, the drop in $h4$ at $-750''$ is not as pronounced. Outside of $1000''$, the values of $h4$ stay roughly constant at larger values, ≈ 0.01 for positive radii and ≈ 0.07 for negative radii. B/P bulges often show dips in the very center in $h4$ (Debattista et al. 2005; M3endez-Abreu et al. 2008), however, this only applies to low inclinations of $i < 30^\circ$. It is therefore not surprising that we do not see a central drop in $h4$ in M31.

5.2. Bar signatures in the gas kinematics and morphology

The simulations of Athanassoula & Beaton (2006) and B17 do not take into account the gas content in M31. However, the gas content in M31 is estimated to be only $\approx 7\%$ of the stellar mass (Corbelli et al. 2010), so we can safely assume that the gas will follow the potential set by the stellar and dark matter components. A detailed discussion of the gas behavior in this potential is postponed again to a future paper (Bla3na et al. in prep.). As mentioned above, the velocity maps for both gas components display an S-shape in the line of zero velocity. This S-shape is stronger than the twist in the stellar velocity field. Such S-shaped twists in the gas velocity are characteristic of velocity fields with oval distortions or bars (Bosma 1981). Many barred galaxies show them, like NGC 1068 (Emsellem et al. 2006), NGC 1300 (Peterson & Huntley 1980), NGC 2683 (Kuzio de Naray et al. 2009), NGC 3386 (Garc3a-Barreto & Rosado 2001) and NGC 5448 (Fathi et al. 2005).

The region of very low velocities at the edge of the bulge on the near side of the galaxy could be produced by a large scale warp in the gas. Such a warp can project small velocities from further out into the line-of-sight (Melchior & Combes 2011).

In Fig. 28 and 29, position-velocity diagrams are plotted for the gas. We show the gas kinematics in this way to compare with similar diagrams from measurements and simulations of neutral gas, e.g. Chemin et al. (2009) and Athanassoula & Beaton (2006). We cut our maps along the disk major axis at $PA=38^\circ$. At each radius, all points perpendicular to the major axis are plotted. They are color coded, depending on their distance to the major axis along the perpendicular coordinate d . Values on the far side of the major axis are shown in blue, values on the near

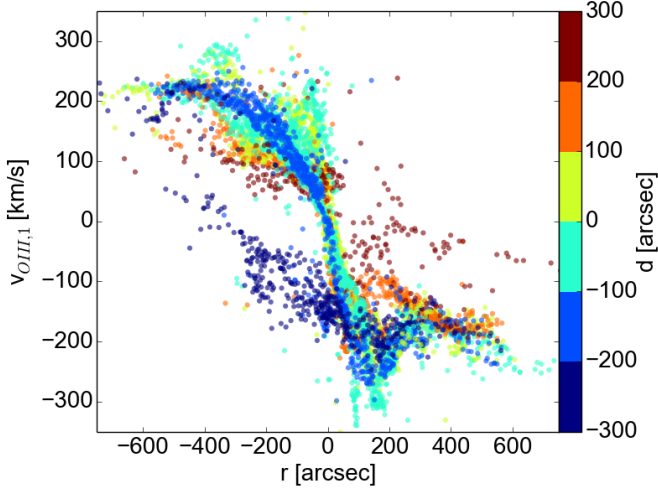


Fig. 28. The position-velocity diagram of the first component projected onto the disk major axis, the x-axis is the distance along the major axis, the y-axis is the velocity and the color represents the perpendicular distance to the major axis.

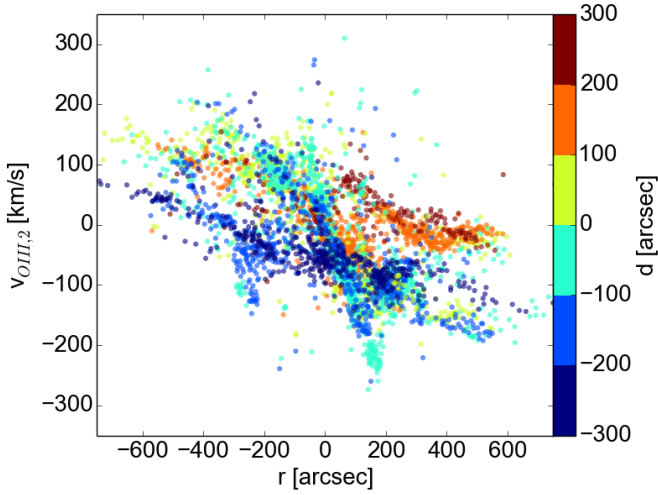


Fig. 29. Similar to Fig. 28, the second component is plotted.

side in red. Fig. 28 shows the first component and Fig. 29 the second one. In this way, differences between the two components become immediately apparent. Both components occupy different regions in the PV-diagrams. The two components are real as they have different velocities. We also compared these PV-diagrams to the ones of the planetary nebulae from Merrett et al. (2006). As expected, neither gas component corresponds to the PNe, since the PNe follow the kinematics of stars.

In the PV-diagram of the first gas component, there is a prominent steep band of velocities in the center. On the receding side, the velocities stay more or less constant once they reach the plateau. The second component also shows a similar steep band of velocities as the first component, but it is less pronounced and much wider. The orange and red points between $0'' < r < 500''$, $0 \text{ km s}^{-1} < v < 100 \text{ km}^{-1}$ and $100'' < d < 200''$ correspond to the arm of zero velocity visible in Fig. 13. To the left of the center, there is an almost flat band of negative velocities, this is the zone of approaching velocities on the eastern side of the bulge in Fig. 13.

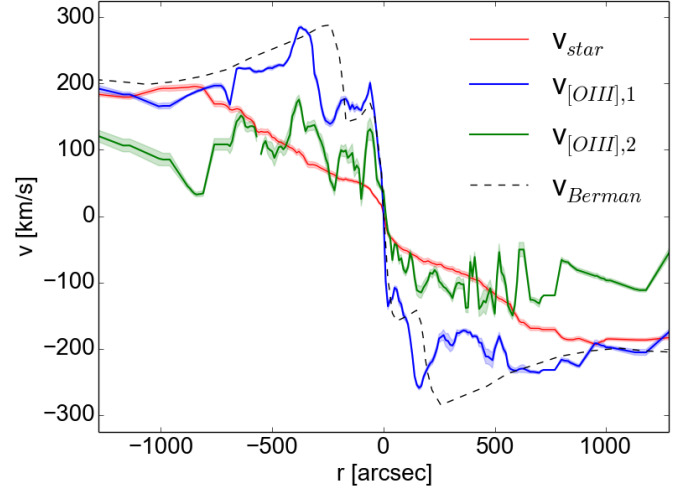


Fig. 30. Cut through the velocity maps along the disk major axis within an aperture of $40''$. The red line is a cut through the stellar velocity (Fig. 6), the blue one is a cut through the first velocity component (Fig. 12), the green one the second velocity component (Fig. 13). The black dashed line is the velocity for the triaxial bar model by Berman (2001).

The position velocity diagram of the first gas component agrees very well with the overall shape of the model of Berman (2001), who simulates a triaxial bulge in M31: the velocity reaches a peak, then stays constant and rises to a second peak. The comparison plot of his data to cuts through our maps is shown in Fig. 30. However, our position-velocity diagrams are asymmetric: for the approaching side of M31 the peak is closer to the center than for the other side. The shape of the PV-diagram could also be compatible with the superposition of other structures, like rings and discs, but this discussion goes beyond the scope of this paper. The overall shape of the position velocity diagram is very similar to what is seen in simulations (Athanasoula & Bureau 1999) and observations of barred galaxies (Bureau & Athanasoula 1999; Merrifield & Kuijken 1999).

The pattern that is visible in the flux maps in [OIII] and $H\beta$ is similar to the one seen by Jacoby et al. (1985) in a $H\alpha$ + [NII] filter and in [OIII], by Boulesteix et al. (1987) in [NII] and by Ciardullo et al. (1988) in $H\alpha$ + [NII]. As seen in section 4.3, the $H\beta$ and [OIII] maps have the overall appearance of a spiral structure, with an incomplete elliptical ring inside, which is oriented roughly along the minor axis, with a “spoke” along the ring’s short axis. The $100''$ long “spoke” along the disk major axis could be an inner disk that is projected due to M31’s inclination and orientation into the elongated shape we see (Jacoby et al. 1985). The inner spiral pattern seems to be tipped to a lower inclination with respect to the outer part, which according to Jacoby et al. (1985) can be caused by a non-axisymmetry, like a bar, and cannot be explained by axisymmetric features alone.

While the ring structure lies in the region where B17 find two inner Lindblad resonances, it is hard to deproject the structures we see in our images. A detailed analysis of the structures is postponed to a later paper, where gas will be taken into account in the dynamical model.

The fact that the incomplete ring is aligned along the minor axis, almost perpendicular to the position of the assumed bar, led Block et al. (2006) to conclude that this ring is not caused by a bar, but by the collision of M31 with M32, which also caused a

“split” of the so-called 10-kpc ring, which is a structure appearing further out in the gas.

While the collision model is in better agreement with the ring structure, especially with the fact that the rings are off-center, it has lower flux inside the ring, whereas in our flux maps, as well as the ones by Jacoby et al. (1985), Boulesteix et al. (1987) and Ciardullo et al. (1988), there is flux present there. We therefore think that the bar is a more likely explanation for the rings. However, as mentioned above, to fully reproduce the visible gas rings, we need to include gas into our bar models, which will be done in the future.

5.3. Bar or triaxial bulge?

The first models that tried to explain the triaxiality in M31 (Stark 1977; Stark & Binney 1994; Berman 2001; Berman & Loinard 2002) called their structures a “triaxial bulge” instead of a “bar”. These two concepts are fundamentally different: A bar is a rotating structure that results from an instability in the disk, while a triaxial bulge is a consequence of an anisotropy in velocity dispersion, generated, e.g. by merging processes. However, as already stated in section 1.3, the models in the aforementioned papers actually describe rapidly rotating systems, which in our understanding are “bars”.

After buckling, most observed bars consist of a three-dimensional inner part of the bar, the B/P-bulge, and a flat outer part (see e.g. Athanassoula 2005 or Martinez-Valpuesta et al. 2006). In this nomenclature, the “triaxial bulge” of the models by Berman (2001) and Berman & Loinard (2002) is a B/P-bulge. Nevertheless, it is still interesting to see if our findings are also consistent with a completely non-rotating structure.

Firstly, we attempt to quantify the level of cylindrical rotation in M31, as cylindrical rotation is generally attributed to the presence of a bar Bureau et al. (2006). Based on Saha & Gerhard (2013), Molaiezhad et al. (2016) (hereafter M16) define the parameter $m_{cyl} = m_{avg} + 1$ where m_{avg} is a measure of the change in rotational velocity in the direction perpendicular to the major axis. m_{avg} averages over the slopes of the decrease in rotational velocity within the bulge region at various distances to the minor axis. M16 first test the discriminatory power of this quantity on data from the Giraffe Inner Bulge Survey Zoccali et al. (2014) of the Milky Way and on a barred N -body model of the Milky Way by Martinez-Valpuesta & Gerhard (2011), and then apply it to 12 further disk galaxies with inclinations ranging from 70° to 90° . They find that the B/P bulges in their sample as well as the Milky Way bulge show levels of cylindrical rotation of $m_{cyl} \approx 0.7$.

As M16 we derive rotation curves parallel and at varying distances to the major axis of M31 first and then turn these into one-sided rotation curves parallel to the minor axis at varying distances to the minor axis. We perform this analysis on the south eastern half of M31 as it is this half where the disk is located on the far side, such that the bulge kinematics are not affected by dust screening of the disk. For the extent of the bulge along the major axis and along the minor axis we adopt values of $460''$ and $270''$ respectively from the bulge to disk decomposition in Kormendy & Bender (1999) and use the photometric disk position angle of 38° (de Vaucouleurs 1958). The resulting plot is shown in Fig. 31. The parameter m_{cyl} for the south-eastern side is 0.72. Changing the exact values of the position angle and also varying the radii for the bulge in major axis direction and in minor axis direction, and also the area of exclusion around the major axis (we use $50''$) have a minor effect on m_{cyl} . Tests show that for reasonable parameter ranges the value never becomes smaller than 0.68. Hence the level of cylindrical rotation — as

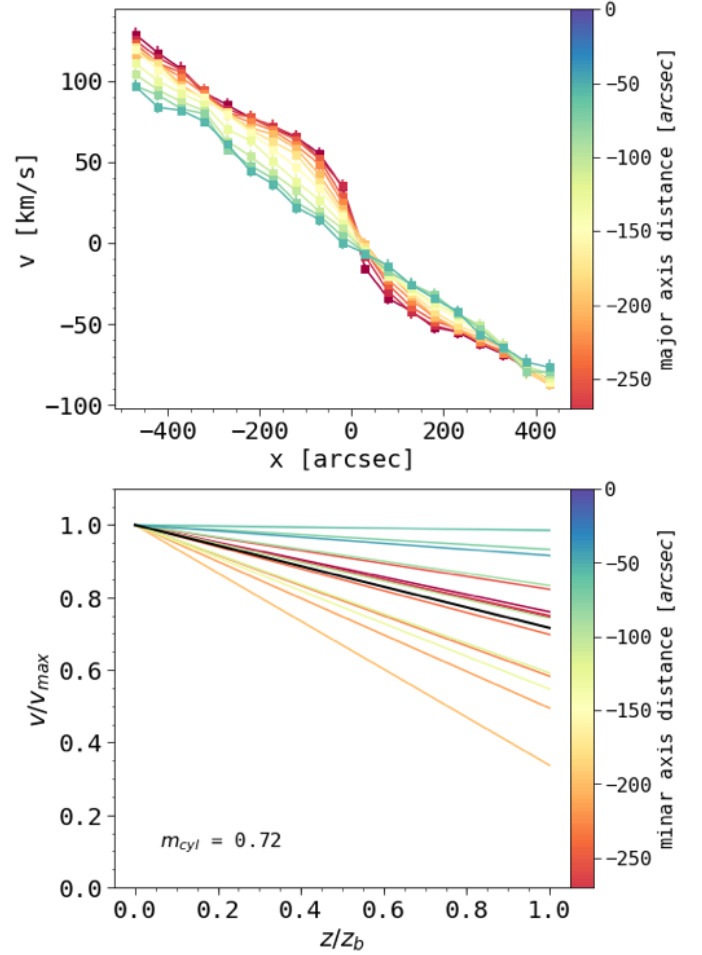


Fig. 31. Measurement of the cylindrical rotation of the south-east side of M31 according to the method by Molaiezhad et al. (2016). Top: The stellar line-of-sight velocity parallel to the major axis of galaxies at different heights from the disk plane. Bottom: The Line-of-sight velocity gradient parallel the minor axis at different distances from the minor axis. Profiles are grey-scale-coded according to the distance from the minor axis. The solid black profile represents the average value m_{avg} . The cylindrical rotation is then $m_{cyl} = m_{avg} + 1$ as a quantity to express the level of cylindrical rotation.

quantified by this method — seems to be consistent to what is reported in Molaiezhad et al. (2016) for their B/P bulges.

Secondly, as described in Athanassoula & Beaton (2006) and B17, the spurs in the photometry outside the bulge argue for a planar bar, the “thin” or “long bar” component described in both papers. Although both papers give different lengths for the thin-bar components, the fact still remains that such a component is required to explain the photometric appearance of the galaxy.

Thirdly, the outer 10 kpc ring of M31 is associated with the outer Lindblad resonance of the bar by B17. This structure is only possible in a rotating barred potential, as there are no characteristic resonance radii in non-rotating triaxial potentials. In a system with a triaxial bulge, this ring would be an ad-hoc feature which is difficult to explain.

Finally, the correlation between v and $h3$ (see Fig. 27) is a clear signature for a bar and not a triaxial bulge.

5.4. Explanations for multiple components

Several scenarios have been suggested by various authors for the origin of the multiple gas components. When gas is subject to a non-axisymmetric potential like a bar, it leads to the formation of gas streams and rings, see e.g. Kim et al. (2012) for numeric models. The line-of-sight passes through several of these streams, therefore leading to multiple peaks in the gas lines. A detailed comparison will only be possible once gas is included into the dynamical model, which will be done in a future paper.

There is also an alternative explanation for such streams and rings in M31, which is that they were created by the collision of M31 with its small companion galaxy M32 (Block et al. 2006). A galaxy with similar inclination as M31, which has also a B/P bulge, is NGC 2683 (Kuzio de Naray et al. 2009). Investigating the $H\alpha$ velocity field, they see S-shaped twists and argue for the presence of a bar at a position angle of 5° higher than the disk position angle. Differences in their PV-diagram and the ones for M31 led Melchior & Combes (2011) to conclude that the interpretation of Athanassoula & Beaton (2006) in terms of a bar in M31 is wrong and that the ring structures are only due to the collision of M31 with M32 suggested by Block et al. (2006). However, the bar in NGC 2683 is only at an angle of 5° to the disk major axis, so it is seen quite side-on, whereas the bar in M31 is at an angle of 17° to the disk major axis and it is seen more end-on, which can explain the differences according to Kuzio de Naray et al. (2009).

Melchior & Combes (2011) also measure molecular emission lines in CO with two peaks, in Melchior & Combes (2016) sometimes even three. While the molecular gas is not expected to follow the ionized gas, it is still interesting that they also observe a line splitting. Melchior & Combes (2011) try to explain the double CO components with a tilted ring model coming from the collision model by Block et al. (2006). An small disk with inclination of 43° , i.e. more face-on than the large-scale disk of M31, is surrounded by a ring. The velocity profiles extracted from the simulated velocity fields by Melchior & Combes (2011) consist of a very broad component, which is blueshifted and a narrow one, which is redshifted, the blueshifted part comes from the inner disk and the redshifted part from the ring. Our [OIII] measurements taken at the same positions look quite different, both components roughly have the same width, so the scenario of Melchior & Combes (2011) does not predict the actual shape of our measured [OIII] spectrum.

Another scenario for multiple components is that large-scale warps in the outer galaxy disk project lower velocities from the outer regions into the inner disk. In the neutral HI gas, Chemin et al. (2009) find up to five different gas components in M31. The velocity maps for all these components look very similar and have basically the same regular kinematic pattern. A component with a steep slope in velocity in the center is the main HI component, while components with flatter slopes are due to slower gas in the outer HI disk that is projected into the central areas due to warps in the HI disk. However Athanassoula & Beaton (2006) find that the different slopes can be explained by the streaming gas motions caused by the bar. Comparing the PV-diagrams of Chemin et al. (2009) with our own, we find that their “main HI component” agrees with the first gas component we measure, while the “zero velocity spiral arm” we measure in the second component agrees with warped components in HI. However, it should be kept in mind that the spatial resolution in Chemin et al. (2009) in the center is less than our own.

5.5. Ionization mechanisms of the gas

In order to investigate which mechanisms are responsible for ionizing the gas, diagnostic diagrams are used, which compare the ratios of line fluxes of different emission lines. The most widely utilized of these diagrams compares $[OIII]\lambda 5007/H\beta$ to $[OI]\lambda 6300/H\alpha$ (Veilleux & Osterbrock 1987). Since we don't have $H\alpha$ or $[OI]\lambda 6300$ in our observed wavelength range, we cannot use this standard diagnostic diagram. Sarzi et al. (2010) devised alternative diagnostic diagrams for the SAURON spectrograph (Bacon et al. 2001), which has a similar wavelength range as VIRUS-W. This diagram compares $[OIII]\lambda 5007/H\beta$ to $[NI]\lambda\lambda 5198, 5200/H\beta$. The [NI] lines are usually present in partially ionized regions in gaseous nebulae, which are photo-ionized by a spectrum containing high-energy photons, but they are absent in HII regions, where $H\beta$ and $[OIII]\lambda 5007$ arise. The Sarzi diagram for the first [OIII] component is shown in Fig. 32, the one for the second component in Fig. 33. There is not much difference between the two diagrams, the datapoints occupy similar regions in both.

The ionization does not happen via starbursts, instead most of the points lie in the region where the ionization is due to shocks in the gas. That shocks are the primary source for ionization is supported by the fact that the emission seems to be strengthened along the lines of the velocity discontinuities. These shocks could be triggered by the bar. About half the points, however, also lie in between the Shock region and the AGN region, which is occupied by Seyfert galaxies in Sarzi et al. (2010), but since the AGN in M31 is very weak (del Burgo et al. 2000), excitation by the AGN is unlikely. These datapoints lying between the regions can be partially explained by the fact that the errors of the datapoints are large. Furthermore, the diagnostic diagram used here does not present as clear separations as the usual $[OI]/H\alpha$ vs. $[OIII]/H\beta$ diagram, compare Sarzi et al. (2006). Contamination by planetary nebulae is also not an issue, we checked the 166 bins that are affected by PNe. They lie in the upper parts of the shock grid and between the shock and the AGN grid, there is no systematic offset of the PNe positions with respect to the rest of our spectra.

6. Conclusions

6.1. Main results

For several decades, the question has been posed if M31 is a barred galaxy or not (Lindblad 1956; Stark 1977; Stark & Binney 1994; Athanassoula & Beaton 2006; B17). The high inclination of M31 made it difficult for a long time to see the bar directly in optical photometry. Twists in the inner isophotes were the first hints for its existence (Lindblad 1956; Stark 1977), while more recently, the boxy appearance of the isophotes in infrared images was used to constrain its orientation and length (Beaton et al. 2007; B17). However, a kinematic confirmation of the bar has been missing so far.

In this paper, we have presented results from observations of M31 with the optical integral field unit spectrograph VIRUS-W. We derive the kinematic properties of the stars and two different ionized gas components and measure the gas fluxes. We find hints in the kinematics that M31 contains a bar. Our main results are:

1. Cuts through the stellar velocity field reveal a plateau at moderate radii, which is a signature that can be created by a bar that is seen at an intermediate angle (Bureau & Athanassoula 2005). The line of zero velocity does not coincide with the

- photometric minor axis and shows a twist towards the edge of the bulge.
2. The stellar velocity dispersion field shows a drop in the center, with two maxima aligned along the minor axis. While this central drop can be caused by inner disk structures or dust in the center (Falcón-Barroso et al. 2006) or the classical bulge (B17), it can also be due to the bar, since the stellar orbits that make up the bar become more circular in the center (Bureau & Athanassoula 2005). There are also two inclined plateaus at intermediate radii in the σ profile, a behavior that is also often seen in barred potentials (Bureau & Athanassoula 2005).
 3. The higher Gauss-Hermite moment $h3$ is anti-correlated with the velocity v in the disk regions and the very center, which is the expected behavior for a disk component (Bender et al. 1994). In the majority of the bulge region, $h3$ is correlated with the velocity v , which can be achieved by elongated motions which occur along the bar direction (Bureau & Athanassoula 2005).
 4. The gas kinematics, measured using the [OIII] λ 5007 line, is more complicated than the stellar kinematics. Many spectra exhibit two separate peaks, resulting in two kinematically distinct components. One of the two components has faster velocities than the other one. The fast component has disk-like rotation with a very steep gradient in the center. The line of zero velocity is S-shaped, again pointing to a bar. The overall shape of the rotation curve of the first component is qualitatively in agreement with gas in a barred dynamical model of M31 by Berman (2001).
 5. The position velocity diagrams of the gas components look similar to what is expected from simulations (Athanassoula & Beaton 2006), with arms of steep and flatter slopes. The overall shape of the position-velocity diagram agrees with observations in HI by Chemin et al. (2009). They measure up to 5 different components, the most luminous of which is the main HI disk, which coincides with the steep slope in the position-velocity diagram. The other components belong to the branches with lower slope in the position-velocity diagrams. According to Chemin et al. (2009), they are low velocities from the outer regions of the HI disk, which have been projected to the center due to warps. However, they can also agree with the lower velocity branches that exist in a barred potential (Athanassoula & Beaton 2006).
 6. When looking at the morphology of the gas, we see a spiral pattern, similar to what is seen by Jacoby et al. (1985) in $H\alpha$ +[NII] and [OIII], Boulesteix et al. (1987) in [NII] and Ciardullo et al. (1988) in $H\alpha$ +[NII]. This spiral pattern has a lower inclination than the disk, which means it could have been tilted by a non-axisymmetry, like a bar (Jacoby et al. 1985).
 7. Block et al. (2006) find that the morphology of M31 in the far infrared is not caused by a bar, but is instead the result of a density wave caused by the collision of M32 with M31. Comparing their gas morphology with our measured one, the ring somewhat corresponds to what we see, but there is no high emission inside the ring, which we observe in [OIII]. Building on this model, Melchior & Combes (2011) propose a scenario of a tilted ring in the center over another rotating disk, to explain line splittings they measure in CO observations. Their model predicts that the component in the ring has a very narrow line, while the disk leads to a very broad line, which is not what we see, our two components in that region have the same width. We therefore think that this model does not predict our observations.

8. From diagnostic diagrams for the ionization of the gas, we find that the gas is mostly ionized by shocks and not by starbursts, which is consistent with the low star formation rate of M31 (Davidge et al. 2012). This is also in agreement by the filamentary appearance of the gas morphology, which could be either due to shocks or supernovae of type Ia (Jacoby et al. 1985).

To summarize, there are several hints in the kinematics of the stars and the ionized gas and its morphology for a bar in M31.

6.2. Future work

From the analysis of the absorption line strengths, we measured the age, metallicity and α /Fe-overabundance of the stellar populations. These results will be presented in an accompanying paper (Opitsch et al. in prep.). These measurements, combined with the kinematics presented in this paper, are used as a basis for a made-to-measure dynamical model (Blaña et al. in prep.). This model will allow us to truly test the bar hypothesis and to check if our observations are caused by the bar, especially once gas is taken into account. They will also provide new estimates on the number of microlensing events caused by MACHOs or self-lensing, which will be used in future microlensing surveys towards M31. We also plan to observe further pointings along the bar major axis, to calculate the pattern speed of the bar.

References

- Adams, J. J., Blanc, G. A., Hill, G. J., et al. 2011, *ApJS*, 192, 5
Afonso, C., Albert, J. N., Andersen, J., et al. 2003, *A&A*, 400, 951
Alcock, C., Akerlof, C. W., Allsman, R. A., et al. 1993, *Nature*, 365, 621
Alcock, C., Allsman, R. A., Alves, D. R., et al. 2000, *ApJ*, 542, 281
Allen, M. G., Groves, B. A., Dopita, M. A., Sutherland, R. S., & Kewley, L. J. 2008, *ApJS*, 178, 20
Athanassoula, E. 2005, *MNRAS*, 358, 1477
Athanassoula, E. & Beaton, R. L. 2006, *MNRAS*, 370, 1499
Athanassoula, E. & Bureau, M. 1999, *ApJ*, 522, 699
Athanassoula, E. & Misiriotis, A. 2002, *MNRAS*, 330, 35
Aubourg, E., Bareyre, P., Bréhin, S., et al. 1993, *Nature*, 365, 623
Bacon, R., Copin, Y., Monnet, G., et al. 2001, *MNRAS*, 326, 23
Barazza, F. D., Jogee, S., & Marinova, I. 2008, *ApJ*, 675, 1194
Barmby, P., Ashby, M. L. N., Bianchi, L., et al. 2006, *ApJ*, 650, L45
Beaton, R. L., Majewski, S. R., Guhathakurta, P., et al. 2007, *ApJ*, 658, L91
Bender, R., Saglia, R. P., & Gerhard, O. E. 1994, *MNRAS*, 269, 785
Berman, S. 2001, *A&A*, 371, 476
Berman, S. & Loinard, L. 2002, *MNRAS*, 336, 477
Bertone, G. 2010, *Particle Dark Matter : Observations, Models and Searches* (Cambridge University Press)
Binney, J. & Tremaine, S. 1987, *Galactic dynamics*
Binney, J. & Tremaine, S. 2008, *Galactic Dynamics: Second Edition* (Princeton University Press)
Blaña, M., Wegg, C., Gerhard, O., et al. 2017, *ArXiv e-prints*, in press, abbreviated as B17 in the text
Blaña, M., Wegg, C., Gerhard, O., et al. in prep., *MNRAS*
Block, D. L., Bournaud, F., Combes, F., et al. 2006, *Nature*, 443, 832
Bosma, A. 1981, *AJ*, 86, 1825
Boulesteix, J., Georgelin, Y. P., Lecoarer, E., Marcelin, M., & Monnet, G. 1987, *A&A*, 178, 91
Brinks, E. & Burton, W. B. 1984, *A&A*, 141, 195
Brinks, E. & Shane, W. W. 1984, *A&AS*, 55, 179
Bureau, M., Aronica, G., Athanassoula, E., et al. 2006, *MNRAS*, 370, 753
Bureau, M. & Athanassoula, E. 1999, *ApJ*, 522, 686
Bureau, M. & Athanassoula, E. 2005, *ApJ*, 626, 159
Cappellari, M. & Copin, Y. 2003, *MNRAS*, 342, 345
Cappellari, M. & Emsellem, E. 2004, *PASP*, 116, 138
Chemin, L., Carignan, C., & Foster, T. 2009, *ApJ*, 705, 1395
Chung, A. & Bureau, M. 2004, *AJ*, 127, 3192
Ciardullo, R., Rubin, V. C., Ford, Jr., W. K., Jacoby, G. H., & Ford, H. C. 1988, *AJ*, 95, 438
Combes, F., Debbsch, F., Friedli, D., & Pfenniger, D. 1990, *A&A*, 233, 82
Combes, F. & Sanders, R. H. 1981, *A&A*, 96, 164

- Comerón, S., Knapen, J. H., & Beckman, J. E. 2008, *A&A*, 485, 695
- Corbelli, E., Lorenzoni, S., Walterbos, R., Braun, R., & Thilker, D. 2010, *A&A*, 511, A89
- Courteau, S., Widrow, L. M., McDonald, M., et al. 2011, *ApJ*, 739, 20
- Dalcanton, J. J., Williams, B. F., Lang, D., et al. 2012, *ApJS*, 200, 18
- Davidge, T. J., McConnachie, A. W., Fardal, M. A., et al. 2012, *ApJ*, 751, 74
- de Grijs, R. & Bono, G. 2014, *AJ*, 148, 17
- de Vaucouleurs, G. 1958, *ApJ*, 128, 465
- de Vaucouleurs, G., de Vaucouleurs, A., Corwin, Jr., H. G., et al. 1991, Third Reference Catalogue of Bright Galaxies. Volume I: Explanations and references. Volume II: Data for galaxies between 0^h and 12^h . Volume III: Data for galaxies between 12^h and 24^h .
- Debattista, V. P., Carollo, C. M., Mayer, L., & Moore, B. 2005, *ApJ*, 628, 678
- del Burgo, C., Mediavilla, E., & Arribas, S. 2000, *ApJ*, 540, 741
- Dopita, M. A., Kewley, L. J., Heisler, C. A., & Sutherland, R. S. 2000, *ApJ*, 542, 224
- Draine, B. T., Aniano, G., Krause, O., et al. 2014, *ApJ*, 780, 172
- Emsellem, E., Fathi, K., Wozniak, H., et al. 2006, *MNRAS*, 365, 367
- Erwin, P. & Debattista, V. P. 2016, *ApJ*, 825, L30
- Eskridge, P. B., Frogel, J. A., Pogge, R. W., et al. 2000, *AJ*, 119, 536
- Fabircius, M. H., Coccatto, L., Bender, R., et al. 2014, *MNRAS*, 441, 2212
- Fabircius, M. H., Grupp, F., Bender, R., et al. 2012a, in Society of Photo-Optical Instrumentation Engineers (SPIE) Conference Series, Vol. 8446, Society of Photo-Optical Instrumentation Engineers (SPIE) Conference Series
- Fabircius, M. H., Saglia, R. P., Fisher, D. B., et al. 2012b, *ApJ*, 754, 67
- Falcón-Barroso, J., Bacon, R., Bureau, M., et al. 2006, *MNRAS*, 369, 529
- Fathi, K., van de Ven, G., Peletier, R. F., et al. 2005, *MNRAS*, 364, 773
- Fisher, D. 1997, *AJ*, 113, 950
- Fritz, J., Gentile, G., Smith, M. W. L., et al. 2012, *A&A*, 546, A34
- Ganda, K., Falcón-Barroso, J., Peletier, R. F., et al. 2006, *MNRAS*, 367, 46
- García-Barreto, J. A. & Rosado, M. 2001, *AJ*, 121, 2540
- Gerhard, O. E. 1993, *MNRAS*, 265, 213
- Gerhard, O. E. & Wegg, C. 2015, in Lessons from the Local Group - A Conference in honour of David Block and Bruce Elmegreen, ed. K. Freeman, B. Elmegreen, D. Block, & M. Woolway (Berlin Heidelberg New York: Springer-Verlag)
- Gilbert, K. M., Guhathakurta, P., Beaton, R. L., et al. 2012, *ApJ*, 760, 76
- Gilbert, K. M., Guhathakurta, P., Kalirai, J. S., et al. 2006, *ApJ*, 652, 1188
- Gilbert, K. M., Guhathakurta, P., Kollipara, P., et al. 2009, *ApJ*, 705, 1275
- Gilbert, K. M., Kalirai, J. S., Guhathakurta, P., et al. 2014, *ApJ*, 796, 76
- Gordon, K. D., Bailin, J., Engelbracht, C. W., et al. 2006, *ApJ*, 638, L87
- Gössl, C. A. & Riffeser, A. 2002, *A&A*, 381, 1095
- Griest, K. 1991, *ApJ*, 366, 412
- Groves, B. A. & Allen, M. G. 2010, *New A*, 15, 614
- Groves, B. A., Dopita, M. A., & Sutherland, R. S. 2004, *ApJS*, 153, 75
- Guhathakurta, P., Ostriker, J. C., Gilbert, K. M., et al. 2005, *ArXiv Astrophysics e-prints*, astro-ph/0502366
- Guhathakurta, P., Rich, R. M., Reitzel, D. B., et al. 2006, *AJ*, 131, 2497
- Hamadache, C., Le Guillou, L., Tisserand, P., et al. 2006, *A&A*, 454, 185
- Henderson, A. P. 1979, *A&A*, 75, 311
- Hernández-López, I., Athanassoula, E., Mújica, R., & Bosma, A. 2009, in *Revista Mexicana de Astronomía y Astrofísica Conference Series*, Vol. 37, *Revista Mexicana de Astronomía y Astrofísica Conference Series*, 160–162
- Hill, G. J., Gebhardt, K., Komatsu, E., & MacQueen, P. J. 2004, in *American Institute of Physics Conference Series*, Vol. 743, *The New Cosmology: Conference on Strings and Cosmology*, ed. R. E. Allen, D. V. Nanopoulos, & C. N. Pope, 224–233
- Ibata, R. A., Lewis, G. F., Conn, A. R., et al. 2013, *Nature*, 493, 62
- Jacoby, G. H., Ford, H., & Ciardullo, R. 1985, *ApJ*, 290, 136
- Kim, W.-T., Seo, W.-Y., Stone, J. M., Yoon, D., & Teuben, P. J. 2012, *ApJ*, 747, 60
- Kirk, J. M., Gear, W. K., Fritz, J., et al. 2015, *ApJ*, 798, 58
- Kormendy, J. 1988, *ApJ*, 325, 128
- Kormendy, J. & Bender, R. 1999, *ApJ*, 522, 772
- Kormendy, J., Drory, N., Bender, R., & Cornell, M. E. 2010, *ApJ*, 723, 54
- Kormendy, J., Fisher, D. B., Cornell, M. E., & Bender, R. 2009, *ApJS*, 182, 216
- Kuzio de Naray, R., Zagsky, M. J., & McGaugh, S. S. 2009, *AJ*, 138, 1082
- Le Borgne, J.-F., Bruzual, G., Pelló, R., et al. 2003, *A&A*, 402, 433
- Lee, C.-H., Koppenhoefer, J., Seitz, S., et al. 2014a, *ApJ*, 797, 22
- Lee, C.-H., Riffeser, A., Koppenhoefer, J., et al. 2012, *AJ*, 143, 89
- Lee, C.-H., Riffeser, A., Seitz, S., Bender, R., & Koppenhoefer, J. 2015, *ApJ*, 806, 161
- Lee, C.-H., Seitz, S., Kodric, M., et al. 2014b, *ApJ*, 785, 11
- Leitherer, C., Schaerer, D., Goldader, J. D., et al. 1999, *ApJS*, 123, 3
- Lindblad, B. 1956, *Stockholms Observatoriums Annaler*, 19
- Martinez-Valpuesta, I. & Gerhard, O. 2011, *ApJ*, 734, L20
- Martinez-Valpuesta, I., Shlosman, I., & Heller, C. 2006, *ApJ*, 637, 214
- McConnachie, A. W., Irwin, M. J., Ibata, R. A., et al. 2009, *Nature*, 461, 66
- Meeks, M. L. 1976, *Methods of experimental physics*. Vol. 12. Astrophysics. Part. C: Radio observations.
- Melchior, A.-L. & Combes, F. 2011, *A&A*, 536, A52
- Melchior, A.-L. & Combes, F. 2016, *A&A*, 585, A44
- Méndez-Abreu, J., Corsini, E. M., Debattista, V. P., et al. 2008, *ApJ*, 679, L73
- Menéndez-Delmestre, K., Sheth, K., Schinnerer, E., Jarrett, T. H., & Scoville, N. Z. 2007, *ApJ*, 657, 790
- Merrett, H. R., Merrifield, M. R., Douglas, N. G., et al. 2006, *MNRAS*, 369, 120
- Merrifield, M. R. & Kuijken, K. 1999, *A&A*, 345, L47
- Merritt, D. & Sellwood, J. A. 1994, *ApJ*, 425, 551
- Molaeinezhad, A., Falcón-Barroso, J., Martínez-Valpuesta, I., et al. 2016, *MNRAS*, 456, 692
- Müller, F. 2014, Development Of A Fiber Based Integral Field Unit and Derivation Of The Instrumental Response Function Of An Existing Integral Field Unit
- Oke, J. B. 1990, *AJ*, 99, 1621
- Opitsch, M., Fabricius, M., Saglia, R., & Bender, R. in prep.
- Paczynski, B. 1986, *ApJ*, 304, 1
- Peiris, H. V. & Tremaine, S. 2003, *ApJ*, 599, 237
- Peterson, C. J. & Huntley, J. M. 1980, *ApJ*, 242, 913
- Planck Collaboration, Ade, P. A. R., Aghanim, N., et al. 2014, *A&A*, 571, A16
- Planck Collaboration, Ade, P. A. R., Aghanim, N., et al. 2016, *A&A*, 594, A13
- Prugniel, P., Soubiran, C., Koleva, M., & Le Borgne, D. 2007, *VizieR Online Data Catalog*, 3251, 0
- Raha, N., Sellwood, J. A., James, R. A., & Kahn, F. D. 1991, *Nature*, 352, 411
- Riffeser, A. in prep.
- Riffeser, A., Fliri, J., Seitz, S., & Bender, R. 2006, *ApJS*, 163, 225
- Rubin, V. C. & Ford, Jr., W. K. 1970, *ApJ*, 159, 379
- Rubin, V. C. & Ford, Jr., W. K. 1971, *ApJ*, 170, 25
- Saglia, R. P., Fabricius, M., Bender, R., et al. 2010, *A&A*, 509, A61, abbreviated as S10 in the text
- Saha, K. & Gerhard, O. 2013, *MNRAS*, 430, 2039
- Sarzi, M., Falcón-Barroso, J., Davies, R. L., et al. 2006, *MNRAS*, 366, 1151
- Sarzi, M., Shields, J. C., Schawinski, K., et al. 2010, *MNRAS*, 402, 2187
- Sellwood, J. A. 2013, in *Planets, Stars and Stellar Systems. Volume 5: Galactic Structure and Stellar Populations*, ed. T. D. Oswalt & G. Gilmore (Berlin Heidelberg New York: Springer-Verlag)
- Sellwood, J. A. & Wilkinson, A. 1993, *Reports on Progress in Physics*, 56, 173
- Smith, M. W. L., Eales, S. A., Gomez, H. L., et al. 2012, *ApJ*, 756, 40
- Stark, A. A. 1977, *ApJ*, 213, 368
- Stark, A. A. & Binney, J. 1994, *ApJ*, 426, L31
- Sumi, T., Bennett, D. P., Bond, I. A., et al. 2013, *ApJ*, 778, 150
- Tisserand, P., Le Guillou, L., Afonso, C., et al. 2007, *A&A*, 469, 387
- Tremaine, S. 1995, *AJ*, 110, 628
- Udalski, A., Szymanski, M., Kaluzny, J., Kubiak, M., & Mateo, M. 1992, *Acta Astron.*, 42, 253
- van der Marel, R. P. & Franx, M. 1993, *ApJ*, 407, 525
- van Leeuwen, F. 2007, *A&A*, 474, 653
- Veilleux, S. & Osterbrock, D. E. 1987, *ApJS*, 63, 295
- Walterbos, R. A. M. & Kennicutt, Jr., R. C. 1987, *A&AS*, 69, 311
- Wegg, C., Gerhard, O., & Portail, M. 2016, *MNRAS*, 463, 557
- Wenger, M., Ochsnein, F., Egret, D., et al. 2000, *A&AS*, 143, 9
- Widrow, L. M., Perrett, K. M., & Suyu, S. H. 2003, *ApJ*, 588, 311
- Williams, B. F., Lang, D., Dalcanton, J. J., et al. 2014, *ApJS*, 215, 9
- Worthey, G., Faber, S. M., Gonzalez, J. J., & Burstein, D. 1994, *ApJS*, 94, 687
- Wyrykowski, L., Rynkiewicz, A. E., Skowron, J., et al. 2015, *ApJS*, 216, 12
- Wyrykowski, L., Skowron, J., Kozłowski, S., et al. 2011, *MNRAS*, 416, 2949
- Zoccali, M., Gonzalez, O. A., Vasquez, S., et al. 2014, *A&A*, 562, A66

7. Appendix

7.1. Comparison with data from S10

We compare the stellar and gas kinematics measured with VIRUS-W with the ones from S10. S10 observed M31 with a longslit spectrograph along 6 directions, the slit positions are plotted in Fig. 34. We make cuts through our own stellar velocity maps along the slit directions of S10 and compare them with their data in Fig. 35. Our velocities agree within 5% with the ones by S10, except for the minor axis on the near side (positive radii in Fig. 35), where the deviation is about 30%.

The comparison plot for the velocity dispersion is shown in Fig. 36. Overall, our data agree well with the measurements of S10, but we do not reproduce the central spike in σ that is caused

by the supermassive black hole, because we lack resolution in the very central regions. The overall agreement is within 4%.

The comparison for $h3$ can be seen in Fig. 37. The standard deviation of the difference between our values and the ones by S10 is 0.020 - 0.027, which agrees with the root mean square value of the error of the VIRUS- W values.

In Fig. 38, the corresponding cuts for $h4$ are shown. Again, we find good agreement, the standard deviation of the difference between our values and the ones by S10 is 0.02, which agrees with the root mean square of the error of the VIRUS- W values.

We also compare our gas kinematics to the data from S10. The comparison plot is shown in Fig. 39. Generally, the first component agrees with the values from S10. For large radii, the velocity from S10 often lies between both velocity components. This is somewhat expected, because S10 do not resolve the two components, so they measure a broader Gaussian, which incorporates both thin Gaussians from the two components. This broader Gaussian has of course a peak value that is in between the two thin ones, which is then adopted as the velocity.

The gas velocity dispersions of S10 are affected by the relatively poor spectral resolution ($\approx 69 \text{ km s}^{-1}$) and tend to be systematically larger than our values. Overall, our data agree very well with S10.

Table 1. Lines used for wavelength calibration

Wavelength Å	Ionization state
4837.314	Ne I
4863.081	Ne I
4884.917	Ne I
4916.068	Hg I
4957.036	Ne I
5005.159	Ne I
5025.600	Hg II
5031.348	Ne I
5037.751	Ne I
5074.201	Ne I
5080.383	Ne I
5113.672	Ne I
5116.503	Ne I
5122.257	Ne I
5144.938	Ne I
5151.961	Ne I
5188.612	Ne I
5203.896	Ne I
5208.865	Ne I
5222.352	Ne I
5234.027	Ne I
5298.190	Ne VI
5330.778	Ne I
5341.094	Ne I
5343.283	Ne I
5400.562	Ne I
5433.651	Ne I

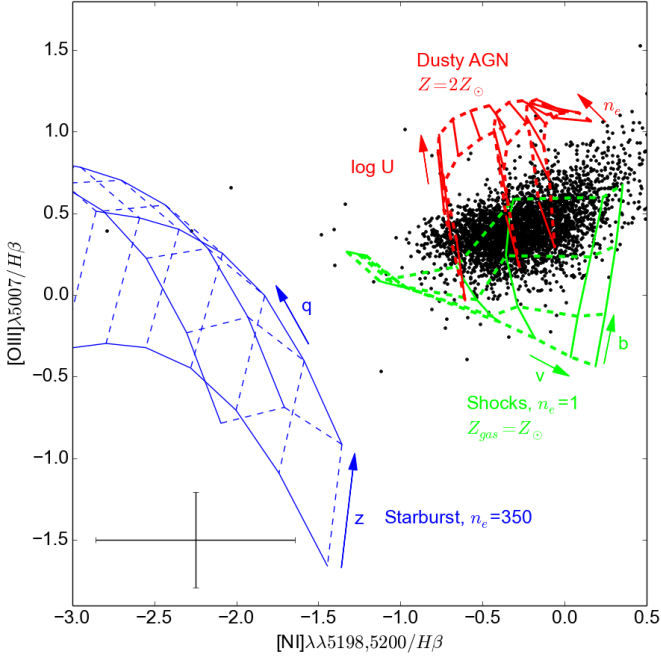


Fig. 32. The diagnostic diagram for the first gas component. The plot is equivalent to the right panel of Fig.1 in Sarzi et al. (2010). The black points are the values from our data. The median error values of the errorbars are shown in the lower left corner. Overplotted are lines showing the predictions for gas that is photoionised by a central AGN, by O-stars or by shocks, respectively. The AGN grids are from the dusty, radiation pressure-dominated models of Groves et al. (2004) and adopt three values for the index α of the power-law AGN continuum $f_\nu \propto \nu^\alpha$, with $\alpha = -1.7, -1.4, -1.2$ from left to right. In each AGN model grid, the solid lines trace the dimensionless ionization parameter $\log U$ (defined as $\log q/c$, which increases with the $[\text{OIII}]/\text{H}\beta$ ratio from $\log U = -3.0, -2.6, -2.3, -2.0, -1.6, -1.3, -1.0$, whereas the dashed lines show the adopted values for the electron density of $N_e = 10^2$ and 10^4 cm^{-3} , with smaller values of the $[\text{NI}]/\text{H}\beta$ ratio corresponding to larger N_e values. The starburst grids are from Dopita et al. (2000), and assume a gas density of $N_e = 350 \text{ cm}^{-3}$ and use a spectral energy distribution obtained from models from Starburst99 (Leitherer et al. 1999) for an instantaneous star formation episode. The grids assume a range of metallicity Z for both stars and gas in the starburst, shown by the solid lines for $Z = 0.2, 0.4, 1.0, 2.0 Z_\odot$, and different values for the ionization parameter q , shown by the dashed lines for $q = 0.5, 1, 2, 4, 8, 15, 30 \times 10^7 \text{ cm s}^{-1}$. The shock grids, without precursor HII region, are from Allen et al. (2008) and assume an electron density of $N_e = 1 \text{ cm}^{-3}$ and a solar value for the gas metallicity. The solid lines show models with increasing shock velocity $v = 150, 200, 300, 500, 750, 1000 \text{ km s}^{-1}$, and the dashed lines models with magnetic parameter $b = 0.5, 1.0, 2.0, 4.0$. The grids have been obtained using the program ITERA (Groves & Allen 2010). We assume solar metallicity for the shocks and twice solar metallicity for the dusty AGN grids, because we obtain these values in the bulge in our stellar population measurements, which will be presented in Opitsch et al. (in prep.).

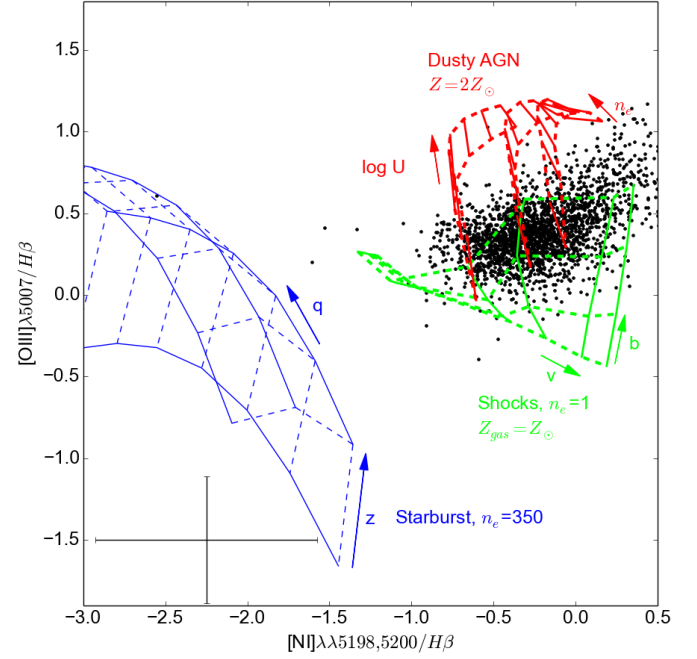


Fig. 33. The diagnostic diagram for the second component. The plot is equivalent Fig. 32, with the grids being the same.

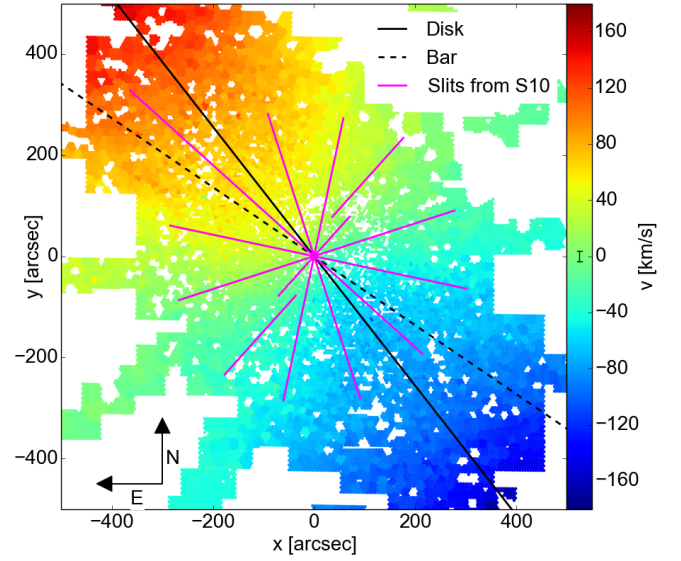


Fig. 34. Velocity map with disk major axis (PA=38°, solid black line), the bar major axis (PA=55.7°, dashed black line) and the slit positions by S10 (magenta). They are PA=48° (the bulge major axis), PA=78°, PA=108°, PA=138° (the bulge minor axis), PA=108° and PA=18°, all angles measured east from north. The line in the colorbar is the median errorbar of the velocities.

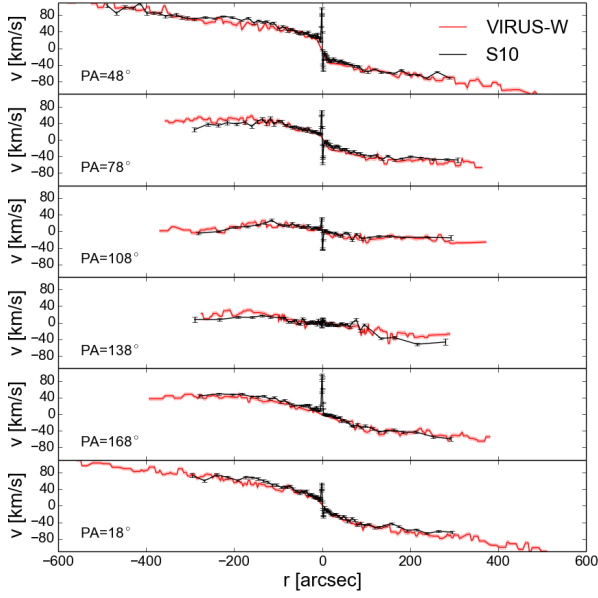


Fig. 35. Comparison of our velocities with the ones from S10. Black are the velocities measured by S10, red are cuts through our velocity maps along the same directions.

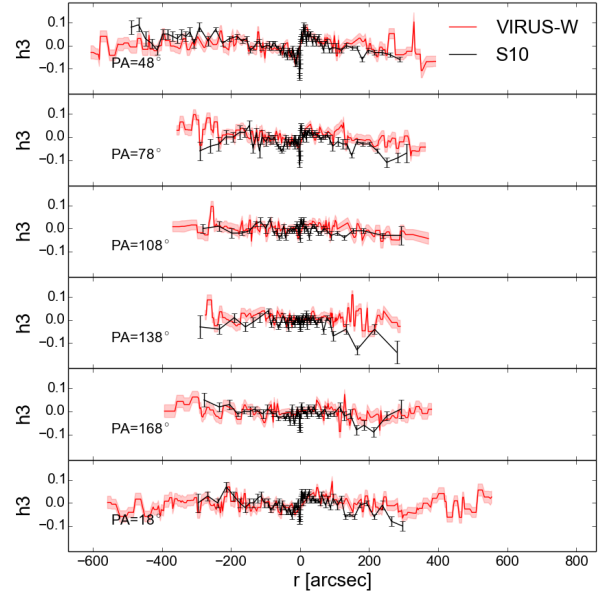


Fig. 37. Comparison of the measured $h3$ values with the ones from S10. Black are the values measured by S10, red are cuts through our maps along the same directions.

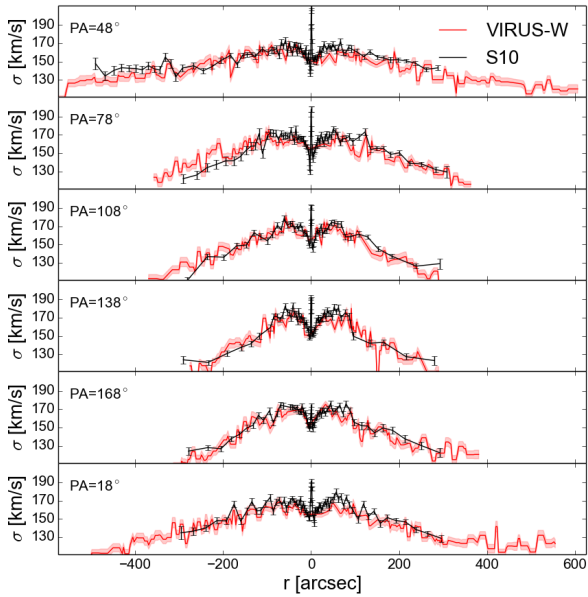


Fig. 36. Comparison of our velocity dispersions with the ones from S10. Black are the values measured by S10, red are cuts through our velocity dispersion maps along the same directions.

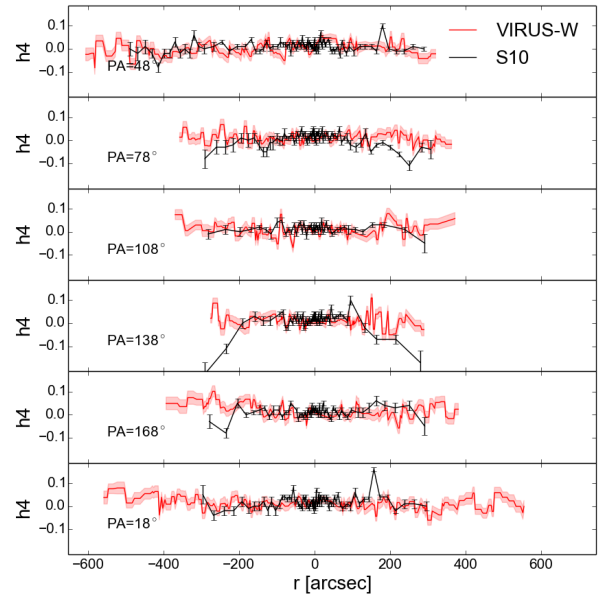


Fig. 38. Comparison of the measured $h4$ values with the ones from S10. Black are the values measured by S10, red are cuts through maps along the same directions.

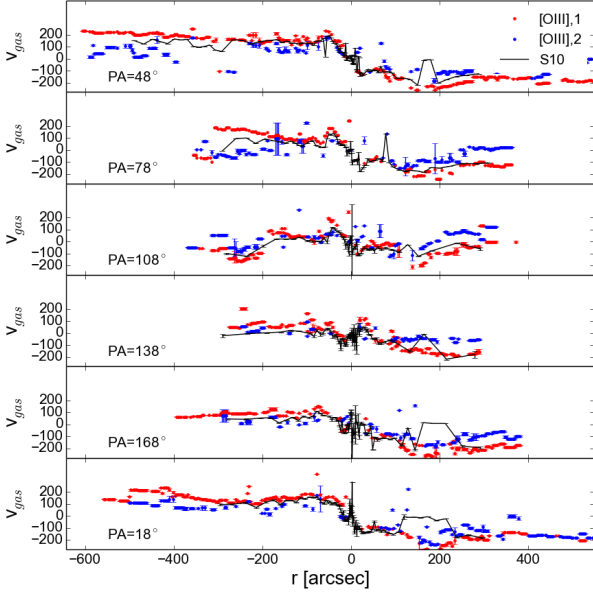


Fig. 39. Comparison of our gas velocities with the ones from S10. Black are the velocities measured by S10, red are cuts through the first gas component from Fig. 12 and blue the cuts through the second component from Fig. 13.

Table 2. Kinematic standard stars, taken from the ELODIE catalog (Prugniel et al. 2007)

HD(...)	Type	RA J2000.0	DEC J2000.0
5516	G8III-IV	00:57:02.0	+23:24:04.0
6203	K0III-IV	01:03:02.5	-04:50:11.8
7010	K0IV	01:11:37.6	+60:30:22.6
10380	K3-IIIb	01:41:25.9	+05:29:15.4
12929	K2IIIab	02:07:10.4	+23:27:44.7
19476	K0III	03:09:16.0	+44:50:51.0
20893	K3III	03:22:45.2	+20:44:31.6
27348	G8III	04:20:12.0	+34:33:33.0
30834	K3III	04:52:25.0	+36:41:53.0
35369	G8III	05:23:47.0	-07:48:37.0
37160	G8III-IV	05:36:44.0	+09:17:35.0
38309	F0III:n	05:42:23.4	+03:59:19.0
39003	K0III	05:51:16.0	+39:08:52.0
39118	G8III+...	05:47:53.9	+02:00:41.4
39833	G0III	05:52:29.1	-00:30:53.9
42787	M2III	06:12:59.5	+06:00:58.5
43039	G8IIIvar	06:15:22.0	+29:29:55.0
45415	G9III	06:27:20.4	+02:54:29.9
46377	K4III	06:30:30.9	+01:18:42.5
46784	M0III	06:32:48.6	+05:33:13.8
48433	K1III	06:43:48.0	+13:13:56.0
54079	K0III:	07:07:49.4	+07:28:16.3
54489	G9III	07:09:07.7	+02:15:11.1
58207	G9III+...	07:25:43.0	+27:47:53.0
58923	F0III	07:28:02.0	+06:56:31.0
61935	K0III	07:41:14.0	-09:33:03.0
62345	G8III	07:44:26.0	+24:23:53.0
62437	F0III	07:41:31.2	+02:31:33.7
72561	G5III	08:31:05.3	+04:55:43.4
76294	G8III-IV	08:55:23.0	+05:56:43.0
81192	G7III	09:24:46.0	+19:47:17.0
94672	F2III	10:53:08.0	+01:00:14.3
104979	G8III	12:05:13.0	+08:43:56.0
120136	F7V	13:47:16.0	+17:27:24.0
122563	F8IV	14:02:32.0	+09:41:14.0
137759	K2III	15:24:55.0	+58:57:57.0
169959	A0III	18:26:52.9	+06:25:24.5
171802	F5III	18:36:27.8	+09:07:21.1
215648	F6III-IV	22:46:41.6	+12:10:22.4

Table 3. Photometric standard stars

Name	Type	RA J2000.0	DEC J2000.0	Reference
BD+284211	Op	21:51:11.1	+28:51:52.0	1
Feige 66	sdO	12:37:23.6	+25:04:00.0	1
Feige 110	D0p	23:19:58.4	-05:09:56.0	1
HD 84937	sdF5	09:48:55.9	+13:44:46.1	2

References. (1) Oke (1990), (2) Le Borgne et al. (2003)

Table 4. Kinematic data of the stars. The full table will be made available online.

Bin Number	RA	DEC	$x[^\circ]$	$y[^\circ]$	v_{star} [km/s]	dv_{star} [km/s]	σ_{star} [km/s]	$d\sigma_{star}$ [km/s]	$h3_{star}$	$dh3_{star}$	$h4_{star}$	$dh4_{star}$
0	00:42:44.23	+41:16:13.98	2.65	4.57	-298.65	1.88	150.80	2.21	0.00	0.01	0.01	0.01
1	00:42:44.46	+41:16:18.55	0.08	9.14	-296.01	2.21	153.82	2.63	0.09	0.01	0.02	0.01
2	00:42:44.27	+41:16:20.78	2.30	11.38	-291.01	2.18	162.39	2.44	-0.02	0.01	0.00	0.01
3	00:42:43.99	+41:16:18.52	5.38	9.11	-292.93	2.43	162.86	2.94	0.02	0.01	0.03	0.01
4	00:42:44.73	+41:16:20.57	-2.92	11.16	-283.70	2.10	155.09	2.52	-0.04	0.01	0.01	0.01
...												

Table 5. Kinematic data of the gas. The full table will be made available online.

Bin Number	$v_{[OIII]}$ [km/s]	$dv_{[OIII]}$ [km/s]	$\sigma_{[OIII]}$ [km/s]	$d\sigma_{[OIII]}$ [km/s]	$v_{[OIII,2]}$ [km/s]	$dv_{[OIII,2]}$ [km/s]	$\sigma_{[OIII,2]}$ [km/s]	$d\sigma_{[OIII,2]}$ [km/s]
0	-	-	-	-	-286.63	5.87	51.05	6.03
1	-322.91	8.02	62.89	7.43	-231.25	6.53	15.61	8.95
2	-327.63	1.56	47.23	1.60	-	-	-	-
3	-364.28	2.06	29.62	2.19	-266.52	4.20	27.97	4.47
4	-140.87	7.29	36.35	7.58	-302.31	1.63	34.70	1.69
...								

Table 6. Photometric data of the gas. The full table will be made available online.

Bin Number	$f_{H\beta}$	$df_{H\beta}$	$f_{[OIII]}$	$df_{[OIII]}$	$f_{[NII]}$	$df_{[NII]}$	$f_{H\beta,2}$	$df_{H\beta,2}$	$f_{[OIII,2]}$	$df_{[OIII,2]}$	$f_{[NII,2]}$	$df_{[NII,2]}$
0	-	-	-	-	-	-	-	-	-	-	-	-
1	2.7	0.4	5.3	0.7	7.4	0.2	0.1	0.1	2.8	0.4	1.1	0.3
2	3.2	0.2	7.1	0.3	1.4	0.2	-	-	0.5	0.3	0.0	0.0
3	1.5	0.2	3.8	0.3	6.6	0.2	1.1	0.2	1.8	0.3	0.3	0.2
4	5.4	0.2	1.1	0.3	0.3	0.2	1.8	0.2	4.4	0.3	0.7	0.2
...												